Electronic Supplementary Information (ESI)

for

Experimental and theoretical investigation on three Dy^{III}_4 single molecule magnets: structural and magneto-structural correlations

Shuvankar Mandal,[a] Abhishek Pramanik,[a] Sourav Dey,[b] Luca M. Carrella,[c] Gopalan Rajaraman,[b]* Eva Rentschler[c]* and Sasankasekhar Mohanta[a]*

[a]*Department of Chemistry*, *University of Calcutta, 92 A. P. C. Road, Kolkata 700 009, India, E-mail*: *sm_cu_chem@yahoo.co.in.*
[b]*Department of Chemistry, Indian Institute of Technology Bombay, Powai, Mumbai 400076, India. Email: rajaraman@chem.iitb.ac.in.*
[c]*Department of Chemistry, Johannes-Gutenberg University Mainz, Duesbergweg 10-14, D-55128 Mainz, Germany. E-mail*: *rentschl@uni-mainz.de*

Table S1. Selected bond angles (º) in the coordination environment in **1**−**3**.

	1	2	3		1	2	3
O1−Dy1−N1	73.7(2)	73.07(19)	73.81(14)	N2−Dy2−O2	134.6(2)	135.41(17)	135.84(13)
O1−Dy1−O5/O5A	91.4(2)	90.72(17)	90.55(14)	N2−Dy2−O5	67.1(2)	68.03(17)	68.14(14)
O1−Dy1−O2/O2A	117.7(2)	115.07(18)	116.06(13)	N2−Dy2−O10	74.5(3)	78.2(2)	78.19(15)
O1−Dy1−O7	151.4(2)	153.20(18)	152.20(13)	N2−Dy2−O9	124.3(3)	125.09(19)	124.02(14)
O1−Dy1−O4	136.1(2)	136.05(17)	136.25(14)	N2−Dy2−O4A/O4	73.3(2)	73.27(17)	73.27(13)
O1−Dy1−O6	76.4(2)	77.65(18)	76.25(14)	N2−Dy2−O7A	132.8(2)	81.98(17)	130.09(12)
O1−Dy1−O8	83.7(2)	84.5(2)	84.79(14)	N2−Dy2−O7	85.3(2)	129.88(16)	83.46(13)
O2/O2A−Dy1−O5/O5A	66.81(19)	67.29(15)	67.16(12)	O2−Dy2−O5	67.58(19)	67.91(15)	68.06(12)
O2/O2A−Dy1−O7	75.68(18)	75.34(14)	75.04(11)	O2−Dy2−O10	105.0(2)	106.45(19)	104.93(15)
O2/O2A−Dy1−O4	80.73(19)	81.10(15)	81.93(12)	O2−Dy2−O9	88.1(2)	87.33(17)	87.08(13)
O2/O2A−Dy1−O6	131.5(2)	130.24(16)	129.43(12)	O2−Dy2−O4A/O4	149.18(19)	147.75(15)	147.86(12)
O2/O2A−Dy1−O8	145.2(2)	150.32(19)	149.87(13)	O2−Dy2−O7A	79.08(19)	77.35(14)	78.45(12)
O2/O2A−Dy1−N1	66.5(2)	65.94(16)	65.29(13)	O2−Dy2−O7	77.75(19)	78.24(15)	76.67(12)
O4−Dy1−O5/O5A	131.80(18)	132.23(14)	132.57(12)	O4A/O4−Dy2−O5	138.65(19)	140.43(16)	140.50(12)
O4−Dy1−O7	67.97(18)	67.89(14)	68.04(12)	O4A/O4−Dy2−O10	94.5(2)	92.3(2)	93.17(15)
O4−Dy1−O6	63.40(19)	62.60(15)	62.89(12)	O4A/O4−Dy2−O9	82.0(2)	82.98(18)	82.92(13)
O4−Dy1−O8	103.1(2)	100.5(2)	98.04(13)	O4A/O4−Dy2−O7A	70.42(19)	96.79(15)	70.15(12)
O4−Dy1−N1	79.8(2)	78.32(17)	79.86(13)	O4A/O4−Dy2−O7	95.05(19)	70.08(15)	98.04(12)
O5/O5A−Dy1−O7	70.04(18)	69.97(14)	69.70(12)	O5−Dy2−O10	86.1(2)	87.73(19)	87.10(14)
O5/O5A−Dy1−O6	161.2(2)	161.87(16)	162.14(12)	O5−Dy2−O9	130.5(2)	126.44(18)	126.04(13)
O5/O5A−Dy1−O8	86.9(2)	91.7(2)	92.60(13)	O5−Dy2−O7A	132.08(18)	70.34(15)	131.95(12)
O5/O5A−Dy1−N1	115.1(2)	116.30(17)	114.96(13)	O5−Dy2−O7	70.86(18)	132.08(15)	69.90(12)
O6−Dy1−O7	114.96(19)	115.64(15)	117.78(13)	O7−Dy2−O7A	69.1(2)	69.89(18)	69.56(13)
O6−Dy1−O8	77.7(2)	73.6(2)	74.50(14)	O7−Dy2−O9	147.1(3)	82.83(17)	150.84(13)
O6−Dy1−N1	75.5(2)	73.88(18)	73.27(13)	O7−Dy2−O10	154.0(2)	135.27(19)	154.73(14)
O7−Dy1−O8	74.0(2)	77.89(19)	77.07(13)	O7A−Dy2−O9	79.2(3)	150.81(17)	83.68(12)
O7−Dy1−N1	133.5(2)	131.71(17)	131.74(13)	O7A−Dy2−O10	136.8(2)	154.77(19)	135.70(13)
O8−Dy1−N1	148.2(2)	143.7(2)	144.64(15)	O9−Dy2−O10	58.4(3)	53.69(19)	53.00(14)

Table S2. The CASSCF/RASSI-SO/SINGLE_ANISO computed energy and g tensors of the eight KDs ($^6H_{15/2}$) of the Dy2A (Fig. S8; Dy_b) centre of complex **1**.

Energy (cm^{-1})	g_x	g_y	g_z	Angle of g_{zz} between ground and first excited KD (°)
0.0	0.121	0.367	18.970	
54.9	0.744	0.955	15.143	12.2
124.2	3.147	3.653	10.822	
185.3	7.392	6.537	1.306	
255.8	2.463	4.048	12.773	
336.9	0.657	1.036	16.435	
402.6	0.233	0.270	19.519	
486.2	0.035	0.068	19.441	

Table S3. The CASSCF/RASSI-SO/SINGLE_ANISO computed energy and g tensors of the eight KDs ($^6H_{15/2}$) of the Dy1 (Fig. S8; Dy_w) centre of complex **1**.

Energy (cm^{-1})	g_x	g_y	g_z	Angle of g_{zz} between ground and first excited KD (°)
0.0	0.013	0.024	19.828	
164.0	0.143	0.252	19.068	15.6
281.6	3.341	4.541	10.963	
341.1	0.202	4.396	10.987	
398.2	3.251	5.661	9.413	
481.8	1.016	3.513	13.294	
518.1	0.559	2.831	13.320	
551.7	1.450	3.085	16.573	

Table S4. The CASSCF/RASSI-SO/SINGLE_ANISO computed energy and g tensors of the eight KDs ($^6H_{15/2}$) of the Dy2 (Fig. S8; Dy_b) centre of complex **1**.

Energy (cm^{-1})	g_x	g_y	g_z	Angle of g_{zz} between ground and first excited KD (°)
0.0	0.121	0.365	18.968	
54.9	0.746	0.956	15.130	12.0
124.2	3.142	3.641	10.814	
185.3	7.400	6.509	1.289	
255.8	2.450	4.050	12.734	
336.9	0.656	1.038	16.408	
402.6	0.232	0.272	19.464	
486.2	0.035	0.068	19.428	

Table S5. The CASSCF/RASSI-SO/SINGLE_ANISO computed energy and g tensors of the eight KDs ($^6H_{15/2}$) of the Dy1A (Fig. S8; Dy_w) centre of complex **1**.

Energy (cm^{-1})	g_x	g_y	g_z	Angle of g_{zz} between ground and first excited KD (°)
0.0	0.013	0.024	19.840	
164.0	0.143	0.253	17.091	15.7
281.6	3.353	4.556	10.969	
341.1	0.197	4.400	11.019	
398.2	3.256	5.674	9.456	
481.8	1.014	3.526	13.356	
518.1	0.561	2.837	13.332	
551.7	1.453	3.080	16.632	

Table S6. The CASSCF/RASSI-SO/SINGLE_ANISO computed energy and g tensors of the eight KDs ($^6H_{15/2}$) of the Dy2 (Fig. S8; Dy_b) centre of complex **2**.

Energy (cm^{-1})	g_x	g_y	g_z	Angle of g_{zz} between ground and first excited KD (°)
0.0	0.080	0.181	18.831	
91.5	2.144	4.835	12.199	7.3
129.8	0.258	5.390	10.791	
188.2	9.185	6.399	1.785	
257.6	1.930	3.442	12.763	
355.1	0.162	1.270	15.421	
371.1	0.574	1.147	18.517	
440.6	0.020	0.043	19.149	

Table S7. The CASSCF/RASSI-SO/SINGLE_ANISO computed energy and g tensors of the eight KDs ($^6H_{15/2}$) of the Dy1 (Fig. S8; Dy_w) centre of complex **2**.

Energy (cm^{-1})	g_x	g_y	g_z	Angle of g_{zz} between ground and first excited KD (°)
0.0	0.009	0.020	19.803	
169.5	0.052	0.162	17.187	19.0
276.6	4.605	5.627	10.183	
323.6	0.776	3.393	13.075	
383.1	1.316	4.872	8.466	
456.2	0.784	4.722	13.829	
508.3	0.488	2.765	13.916	
547.6	1.169	3.192	15.981	

Table S8. The CASSCF/RASSI-SO/SINGLE_ANISO computed energy and g tensors of the eight KDs ($^6H_{15/2}$) of the Dy2A (Fig. S8; Dy_b) centre of complex **2**.

Energy (cm^{-1})	g_x	g_y	g_z	Angle of g_{zz} between ground and first excited KD (°)
0.0	0.080	0.183	18.880	
91.5	2.147	4.861	12.216	7.3
129.8	0.261	5.394	10.847	
188.2	9.193	6.415	1.779	
257.6	1.927	3.451	12.758	
335.0	0.157	1.275	15.421	
371.1	0.578	1.148	18.521	
440.6	0.020	0.043	19.169	

Table S9. The CASSCF/RASSI-SO/SINGLE_ANISO computed energy and g tensors of the eight KDs ($^6H_{15/2}$) of the Dy1A (Fig. S8; Dy_w) centre of complex **2**.

Energy (cm^{-1})	g_x	g_y	g_z	Angle of g_{zz} between ground and first excited KD (°)
0.0	0.009	0.020	19.907	
169.5	0.053	0.161	17.266	18.9
276.6	4.616	5.634	10.202	
323.6	0.799	3.407	13.056	
383.1	1.314	4.873	8.481	
456.2	0.785	4.733	13.883	
508.3	0.492	2.771	13.917	
547.6	1.171	3.202	16.034	

Table S10. The CASSCF/RASSI-SO/SINGLE_ANISO computed energy and g tensors of the eight KDs ($^6H_{15/2}$) of the Dy2A (Fig. S8; Dy_b) centre of complex **3**.

Energy (cm^{-1})	g_x	g_y	g_z	Angle of g_{zz} between ground and first excited KD (°)
0.0	0.209	0.501	18.423	
56.1	2.307	3.763	14.088	45.2
95.0	7.837	5.655	1.021	
158.8	8.750	5.605	1.397	
239.3	1.390	3.181	12.505	
321.8	0.110	1.555	16.020	
359.6	0.642	1.645	16.373	
473.9	0.012	0.017	19.311	

Table S11. The CASSCF/RASSI-SO/SINGLE_ANISO computed energy and g tensors of the eight KDs ($^6H_{15/2}$) of the Dy1 (Fig. S8; Dy_w) centre of complex **3**.

Energy (cm^{-1})	g_x	g_y	g_z	Angle of g_{zz} between ground and first excited KD (°)
0.0	0.009	0.018	19.844	
169.6	0.115	0.181	17.261	17.7
296.2	3.285	4.915	10.663	
351.1	0.812	4.391	12.349	
420.3	2.067	5.038	9.484	
485.6	1.401	5.353	11.204	
522.5	0.938	4.918	11.866	
626.7	0.373	0.509	19.156	

Table S12. The CASSCF/RASSI-SO/SINGLE_ANISO computed energy and g tensors of the eight KDs ($^6H_{15/2}$) of the Dy2 (Fig. S8; Dy$_b$) centre of complex **3**.

Energy (cm^{-1})	g_x	g_y	g_z	Angle of g_{zz} between ground and first excited KD (°)
0.0	0.207	0.499	18.402	
56.1	2.301	3.751	14.037	45.2
94.9	7.811	5.655	1.043	
158.8	8.756	5.590	1.409	
239.3	1.309	3.174	12.521	
321.8	0.109	1.554	16.047	
359.6	0.640	1.639	16.373	
473.9	0.012	0.017	19.286	

Table S13. The CASSCF/RASSI-SO/SINGLE_ANISO computed energy and *g* tensors of the eight KDs ($^6H_{15/2}$) of the Dy1A (Fig. S8; Dy$_w$) centre of complex **3**.

Energy (cm^{-1})	g_x	g_y	g_z	Angle of g_{zz} between ground and first excited KD (°)
0.0	0.009	0.018	19.929	
169.6	0.117	0.181	17.311	17.6
296.2	3.299	4.914	10.671	
351.1	0.791	4.401	12.328	
420.3	2.065	5.035	9.502	
485.6	1.410	5.365	11.203	
522.5	0.939	4.920	11.901	
626.7	0.373	0.511	19.199	

Table S14. The computed crystal field parameter of each metal centres in complex **1**.

k	q	B_k^q			
		Dy2A (Fig. S8; Dy$_b$)	Dy1 (Fig. S8; Dy$_w$)	Dy2 (Fig. S8; Dy$_b$)	Dy1A (Fig. S8; Dy$_w$)
2	-2	-7.21E-01	5.72E-01	-7.21E-01	5.67E-01
	-1	7.57E-01	-1.08E-04	7.58E-01	6.66E-02
	0	-1.96E+00	-2.41E+00	-1.96E+00	-2.41E+00
	1	1.37E-01	2.14E+00	1.11E-01	2.13E+00
	2	1.96E+00	4.10E-01	1.96E+00	4.15E-01
$/\dfrac{Av.\,axial}{Av.\,non-axial}/$		2.19E+00	3.09E+00	2.21E+00	3.03E+00
4	-4	-1.54E-02	-8.23E-03	-1.53E-02	-8.05E-03
	-3	6.52E-02	-2.80E-02	6.55E-02	-2.76E-02
	-2	-8.21E-03	-1.41E-02	-8.31E-03	-1.40E-02
	-1	3.03E-03	-4.34E-03	3.22E-03	-3.64E-03
	0	-7.81E-04	-5.58E-03	-8.02E-04	-5.60E-03
	1	-4.48E-03	8.80E-03	-4.56E-03	8.48E-03
	2	7.97E-03	-3.27E-03	7.71E-03	-3.23E-03
	3	-1.54E-02	-6.07E-02	-1.50E-02	-6.15E-02
	4	-3.32E-02	-1.97E-02	-3.32E-02	-1.99E-02
6	-6	7.03E-05	3.99E-05	6.89E-05	4.15E-05
	-5	-2.66E-04	2.45E-05	-2.65E-04	3.04E-05
	-4	3.55E-05	1.21E-05	3.74E-05	1.55E-05
	-3	5.40E-05	-3.03E-05	5.85E-05	-2.94E-05
	-2	2.05E-04	-1.91E-06	2.06E-04	4.25E-06
	-1	-3.12E-05	-1.19E-05	-3.35E-05	-1.53E-05
	0	1.15E-05	1.07E-05	1.16E-05	1.10E-05
	1	7.62E-05	-3.54E-04	7.62E-05	-3.53E-04
	2	5.43E-05	1.09E-04	5.31E-05	1.08E-04
	3	1.75E-04	-1.17E-04	1.75E-04	-1.15E-04
	4	9.02E-05	-1.63E-04	8.78E-05	-1.63E-04
	5	5.81E-04	-8.92E-04	5.82E-04	-8.93E-04
	6	-1.19E-04	2.00E-04	-1.21E-04	2.00E-04

Table S15. The computed crystal field parameter of each metal centres in complex **2**.

k	q	B_k^q			
		Dy2 (Fig. S8; Dy$_b$)	Dy1 (Fig. S8; Dy$_w$)	Dy2A (Fig. S8; Dy$_b$)	Dy1A (Fig. S8; Dy$_w$)
2	-2	9.61E-01	3.95E-01	9.85E-01	3.92E-01
	-1	-1.07E+00	3.83E-01	-1.09E+00	3.88E-01
	0	-1.09E+00	-2.30E+00	-1.09E+00	-2.29E+00
	1	1.30E+00	-1.82E+00	1.33E+00	-1.82E+00
	2	2.35E+00	7.75E-02	2.34E+00	8.37E-02
$\left/ \dfrac{Av.\,axial}{Av.\,non-axial} \right/$		7.67E-01	5.32E+00	7.59E-01	5.29E+00
4	-4	-4.75E-03	7.13E-03	-4.72E-03	6.64E-03
	-3	8.43E-03	-3.00E-02	9.55E-03	-2.91E-02
	-2	2.37E-02	-1.09E-02	2.36E-02	-1.09E-02
	-1	1.77E-02	-2.79E-03	1.73E-02	-2.66E-03
	0	-4.04E-03	-5.49E-03	-4.02E-03	-5.49E-03
	1	5.96E-03	-9.39E-03	6.09E-03	-9.56E-03
	2	1.09E-02	-1.18E-02	1.07E-02	-1.14E-02
	3	3.82E-02	6.57E-02	3.85E-02	6.69E-02
	4	-3.27E-03	-2.04E-02	-3.17E-03	-2.05E-02
6	-6	-1.26E-04	-2.32E-04	-1.24E-04	-2.31E-04
	-5	6.18E-04	-4.50E-04	6.18E-04	-4.42E-04
	-4	1.11E-05	1.57E-04	9.90E-06	1.55E-04
	-3	3.90E-04	1.63E-05	3.98E-04	1.31E-05
	-2	3.23E-05	6.15E-05	3.25E-05	6.51E-05
	-1	-1.15E-04	6.59E-05	-1.11E-04	6.86E-05
	0	8.55E-07	3.29E-06	1.16E-06	3.27E-06
	1	4.09E-05	3.46E-04	4.83E-05	3.46E-04
	2	6.74E-05	1.60E-04	6.58E-05	1.61E-04
	3	1.68E-04	1.62E-04	1.78E-04	1.69E-04
	4	1.58E-05	-6.68E-05	1.74E-05	-6.99E-05
	5	-1.41E-04	2.08E-04	-1.52E-04	2.23E-04
	6	1.19E-04	1.11E-04	1.22E-04	1.18E-04
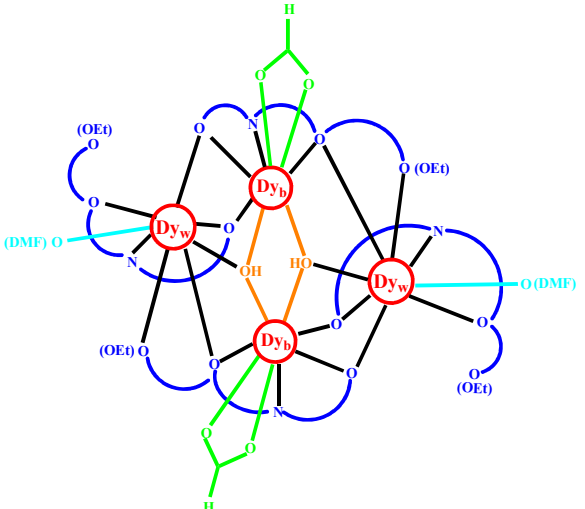
Table S16. The computed crystal field parameter of each metal centres in complex **3**.
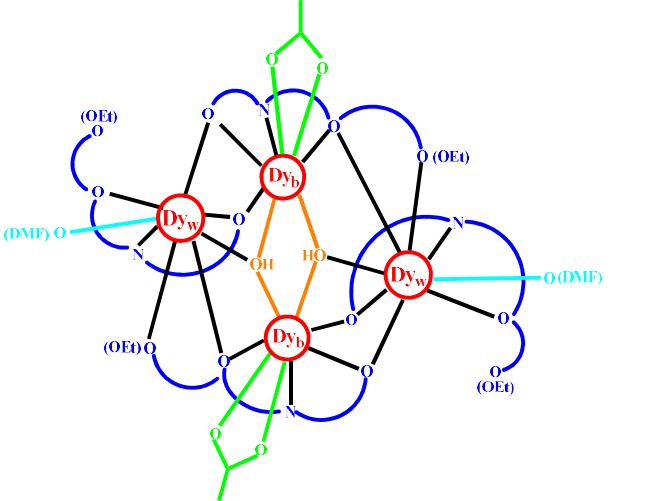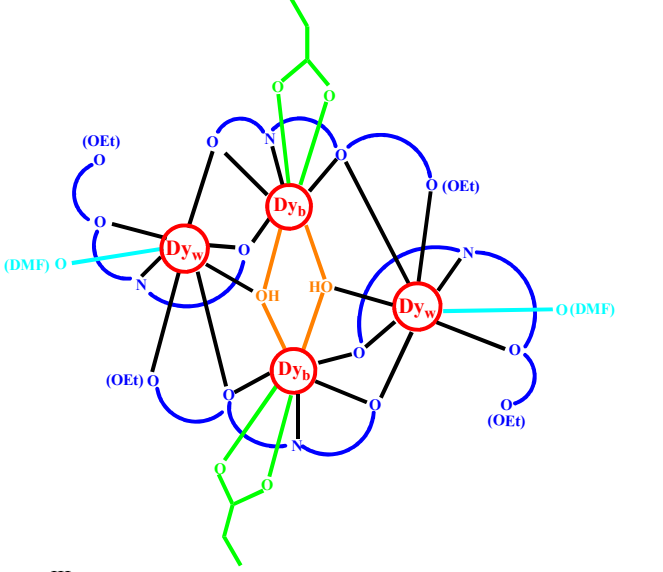
k	q	B_k^q			
		Dy2A (Fig. S8; Dy$_b$)	Dy1 (Fig. S8; Dy$_w$)	Dy2 (Fig. S8; Dy$_b$)	Dy1A (Fig. S8; Dy$_w$)
2	-2	-3.24E-01	1.25E+00	-3.41E-01	1.25E+00
	-1	1.99E+00	4.07E-01	1.98E+00	4.07E-01
	0	-1.16E+00	-2.61E+00	-1.16E+00	-2.61E+00
	1	-1.39E+00	2.12E+00	-1.37E+00	2.11E+00
	2	2.97E+00	2.50E-01	2.96E+00	2.52E-01
$\left/ \overline{\frac{Av.\,axial}{Av.\,non-axial}} \right/$		6.94E-01	2.59E+00	6.98E-01	2.60E+00
4	-4	-1.57E-02	-1.12E-03	-1.56E-02	-1.47E-03
	-3	2.89E-02	-3.64E-03	2.94E-02	-3.82E-03
	-2	1.04E-02	-1.30E-02	1.06E-02	-1.30E-02
	-1	-1.35E-02	-4.98E-04	-1.35E-02	-5.46E-04
	0	-1.86E-03	-5.60E-03	-1.87E-03	-5.59E-03
	1	-1.52E-02	7.46E-03	-1.52E-02	7.51E-03
	2	1.95E-02	-7.62E-03	1.96E-02	-7.33E-03
	3	-6.25E-02	-6.32E-02	-6.24E-02	-6.39E-02
	4	-3.76E-03	-2.26E-02	-3.97E-03	-2.26E-02
6	-6	-1.35E-04	-1.52E-04	-1.35E-04	-1.49E-04
	-5	-1.87E-04	3.33E-04	-1.84E-04	3.17E-04
	-4	-1.24E-04	8.44E-05	-1.22E-04	8.41E-05
	-3	-4.59E-05	-6.34E-05	-4.66E-05	-5.94E-05
	-2	-1.23E-04	3.99E-05	-1.24E-04	4.25E-05
	-1	6.98E-05	-8.78E-05	7.10E-05	-9.25E-05
	0	-1.61E-05	1.15E-05	-1.64E-05	1.13E-05
	1	8.18E-05	-3.55E-04	8.87E-05	-3.58E-04
	2	4.70E-05	1.32E-04	4.73E-05	1.33E-04
	3	-1.26E-04	-9.97E-05	-1.22E-04	-1.08E-04
	4	1.65E-04	-1.02E-04	1.63E-04	-1.03E-04
	5	1.66E-04	-6.18E-04	1.61E-04	-6.31E-04
	6	6.53E-06	2.39E-04	4.56E-06	2.43E-04
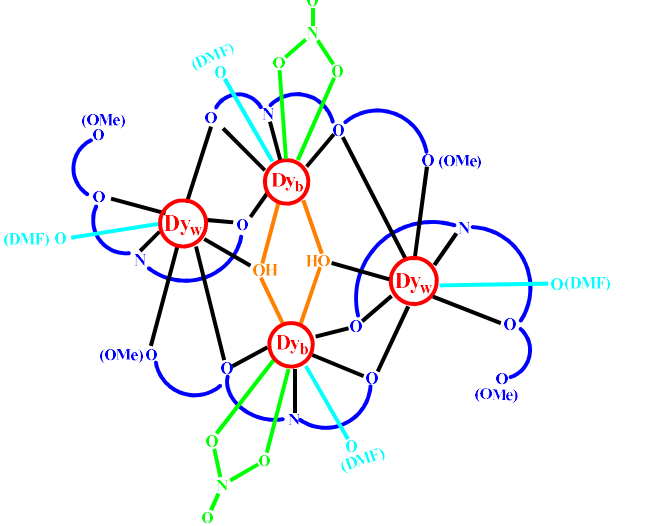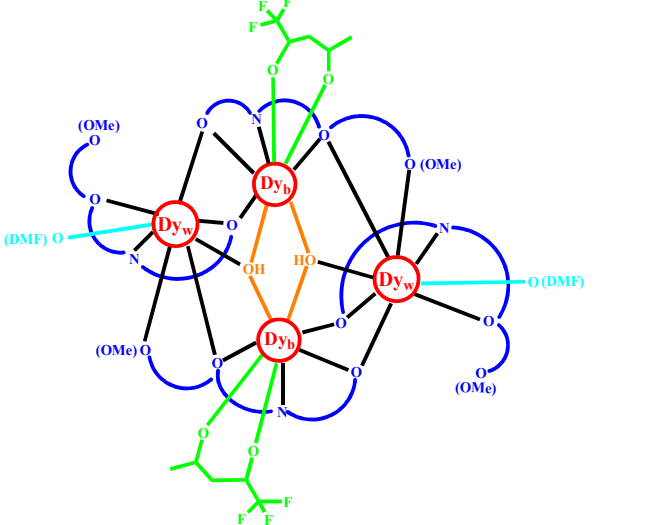
Table S17. A comparison of average Dy−O−Dy angle (°) and symbol for exchange interaction in complexes **1**−**3**.
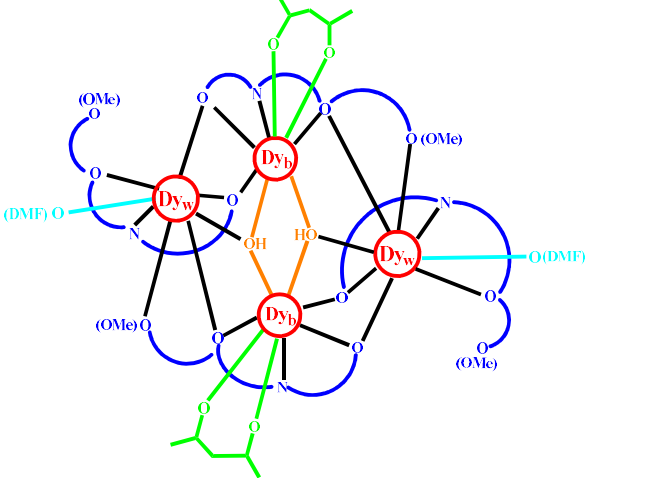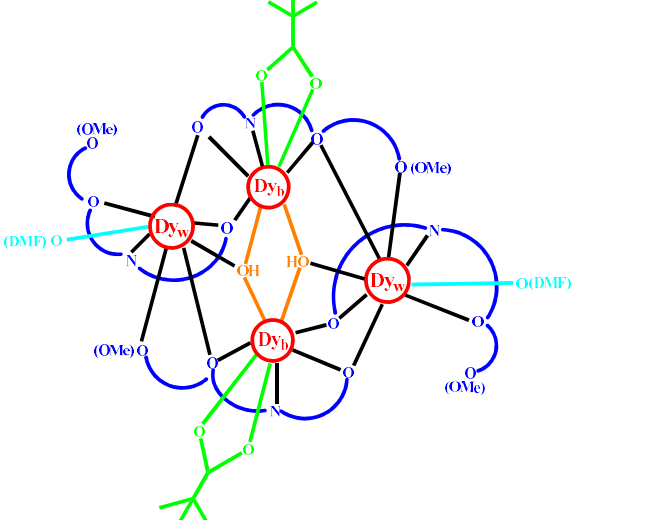
Angle (Atom labels in Fig. S8)	1	2	3	Symbol for exchange interaction in Fig. 12 and text
Dy1−O2/O5/O7−Dy2 (**1** and **3**); Dy1−O2A/O5A/O7−Dy2A (**2**) [Bis(μ-phenoxo)-μ-hydroxo Dy_b−O−Dy_w]	94.9	95.0	95.4	J_{bw1}
Dy1−O4/O7−Dy2A (**1** and **3**); Dy1−O4/O7−Dy2 (**2**) [μ-phenoxo-μ-hydroxo Dy_b−O−Dy_w]	110.8	110.9	110.8	J_{bw2}
Dy1A−O2A/O5A/O7A−Dy2A (**1** and **3**); Dy1A−O2/O5/O7A−Dy2 (**2**) [Bis(μ-phenoxo)-μ-hydroxo Dy_b−O−Dy_w]	94.9	95.0	95.4	J_{bw1}
Dy1A−O4A/O7A−Dy2 (**1** and **3**); Dy1A−O4A/O7A−Dy2A (**2**) [μ-phenoxo-μ-hydroxo Dy_b−O−Dy_w]	110.8	110.9	110.8	J_{bw2}
Dy2−O7/O7A−Dy2A (**1**, **2** and **3**) [Bis(μ-hydroxo) Dy_b−O−Dy_b]	110.9	110.1	110.4	J_{bb}
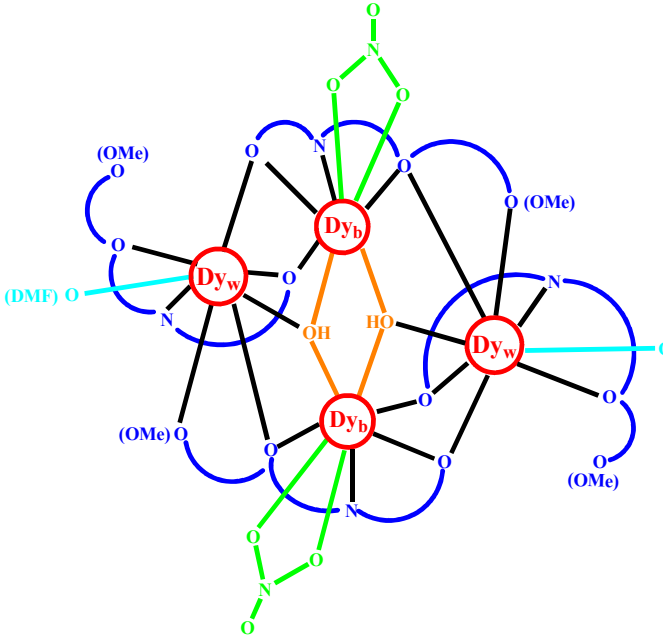
Table S18. Simplified pictorial presentation, formula and magnetic parameters of the Dy^{III}_4 defect dicubane compounds derived from 2-(2-hydroxy-3-ethoxybenzylideneamino)phenol, H_2L (OEt ligand), and 2-(2-hydroxy-3-methoxybenzylideneamino)phenol, H_2L' (OMe ligand).
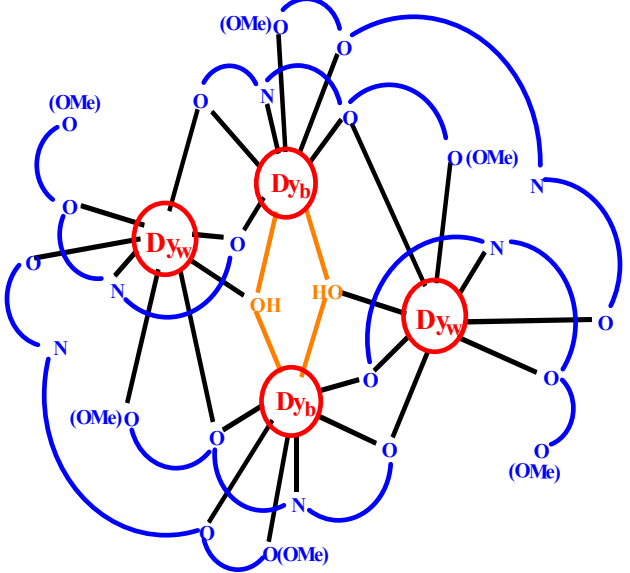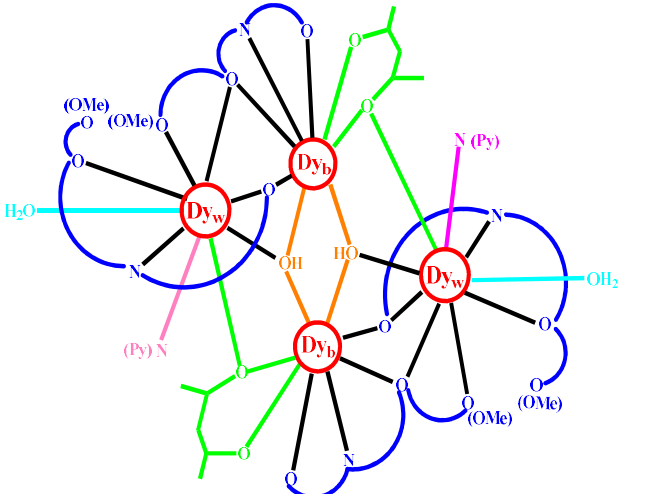
Formula and Simplified Pictorial Presentation	U_{eff}	τ_0	Coordination No.	Two-step relaxation process identified or mentioned	Ref.
[Dy$^{III}_4$L$_4$(μ_3-OH)$_2$(formate)$_2$(dmf)$_2$] **(1)**	49.0 cm^{-1}	1.76×10^{-7} s	8 for Dy$_b$ 8 for Dy$_w$	Yes	This work

[Dy$^{III}_4$L$_4$(μ_3-OH)$_2$(acetate)$_2$(dmf)$_2$] **(2)**	30.3 cm^{-1}	1.51 × 10^{-8} s	8 for Dy$_b$ 8 for Dy$_w$	Yes	This work
[Dy$^{III}_4$L$_4$(μ_3-OH)$_2$(propionate)$_2$(dmf)$_2$] **(3)**	23.4 cm^{-1}	9.64 × 10^{-7} s	8 for Dy$_b$ 8 for Dy$_w$	Yes	This work

 $[Dy^{III}_4L'_4(\mu_3\text{-}OH)_2(dmf)_4(NO_3)_2].2dmf.H_2O$ (**I**)	Could not be evaluated as no maximum for χ_M'' up to 2 K	Could not be evaluated as no maximum for χ_M'' up to 2 K	9 for Dy_b 8 for Dy_w	Not Applicable	S1
 $[Dy^{III}_4L'_4(\mu_3\text{-}OH)_2(dmf)_2(tfaa)_2].2CH_3CN$ (**II**)	27.1 cm^{-1}	2.09×10^{-5} s	8 for Dy_b 8 for Dy_w	Yes	S1

[Dy$^{III}_4$L$'_4$(μ_3-OH)$_2$(dmf)$_2$ (acac)$_2$].2dmf (**III**)	65.3 cm^{-1}	9.62 × 10^{-7} s	8 for Dy$_b$ 8 for Dy$_w$	Yes	S1
[Dy$^{III}_4$L$'_4$(μ_3-OH)$_2$(dmf)$_2$ (trimethylacetate)$_2$].2CH$_3$CN (**IV**)	38.9 cm^{-1}	2.66 × 10^{-8} s	8 for Dy$_b$ 8 for Dy$_w$	Yes	S2

	79.2 cm^{-1}	1.58×10^{-9} s	8 for Dy$_b$	Yes	S3
			8 for Dy$_w$		

$[Dy^{III}_4L'_4(\mu_3\text{-}OH)_2(dmf)_2(NO_3)_2]$ **(V)**

$[Dy^{III}_4L'_4(\mu_3\text{-OH})_2(HL')_2].2THF$ **(VI)**	2.6 cm^{-1}	4.8×10^{-5} s	8 for Dy_b 8 for Dy_w	No	S4
$[Dy^{III}_4L'_4(\mu_3\text{-OH})_2(acac)_2(H_2O)_2(C_5H_5N)_2].2THF$ **(VII)**	25.7 cm^{-1} at 5 K 54.2 cm^{-1} at 13 K	5×10^{-7} s 7×10^{-7} s	8 for Dy_b 9 for Dy_w	Yes	S5
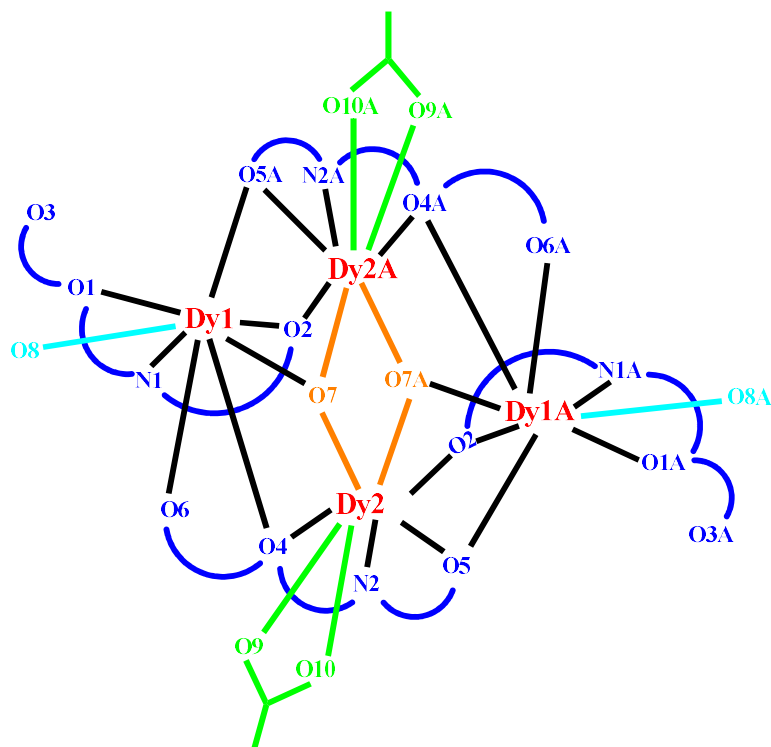
Scheme S1. Simplified schematic presentation of $[Dy^{III}_4L_4(\mu_3\text{-}OH)_2(\text{acetate})_2(\text{dmf})_2]$ (**2**). Colour: Blue – $[L]^{2-}$; Orange – Hydroxo; Green – Carboxylate; Cyan – dmf.
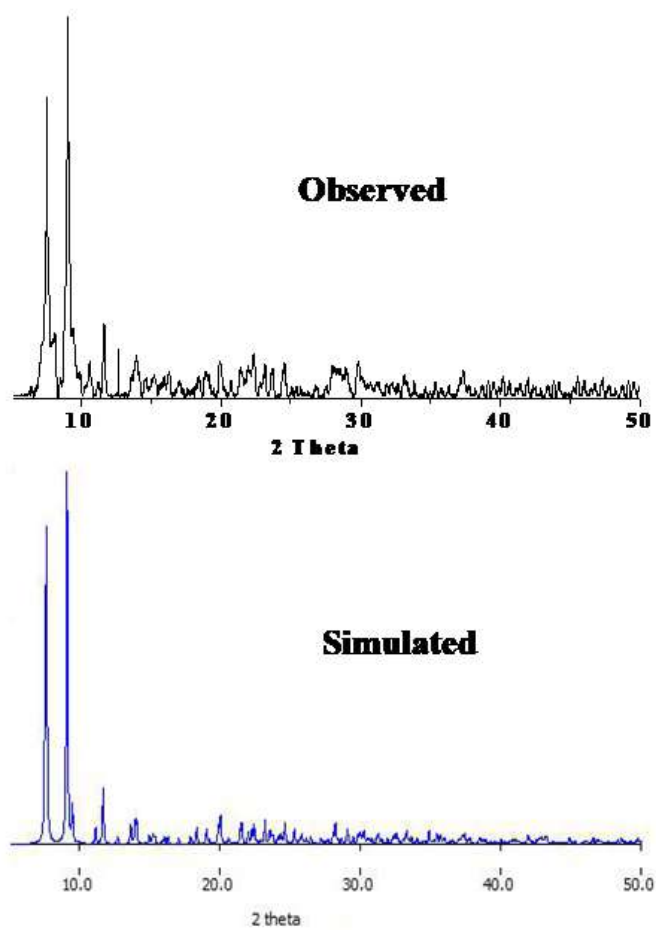
Fig. S1. Simulated (blue) and observed (black) powder X-ray diffraction (PXRD) patterns of $[Dy^{III}_4L_4(OH)_2(formate)_2(dmf)_2]$ (**1**).
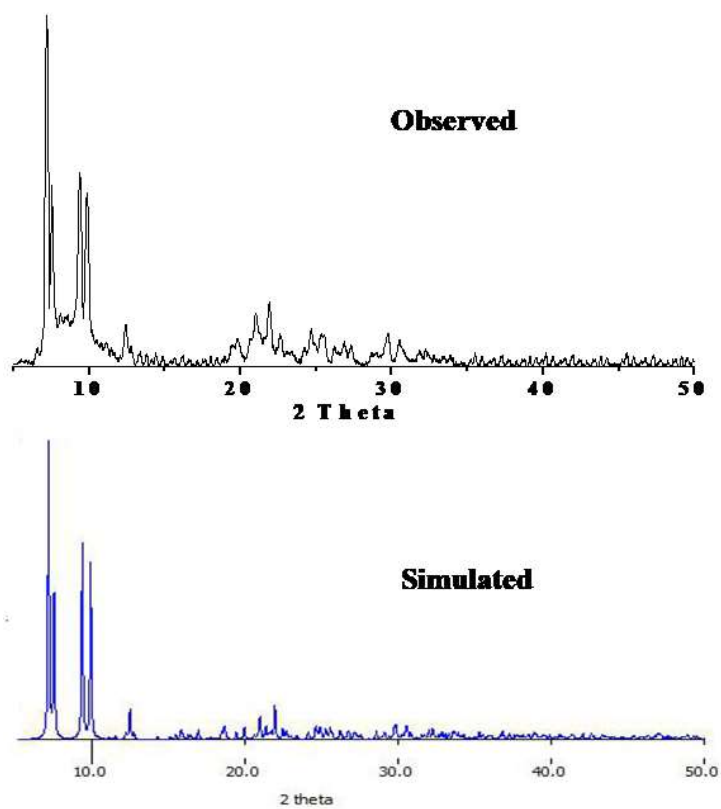
Fig. S2. Simulated (blue) and observed (black) powder X-ray diffraction (PXRD) patterns of $[Dy^{III}_4L_4(\mu_3\text{-OH})_2(\text{acetate})_2(\text{dmf})_2]$ (**2**).
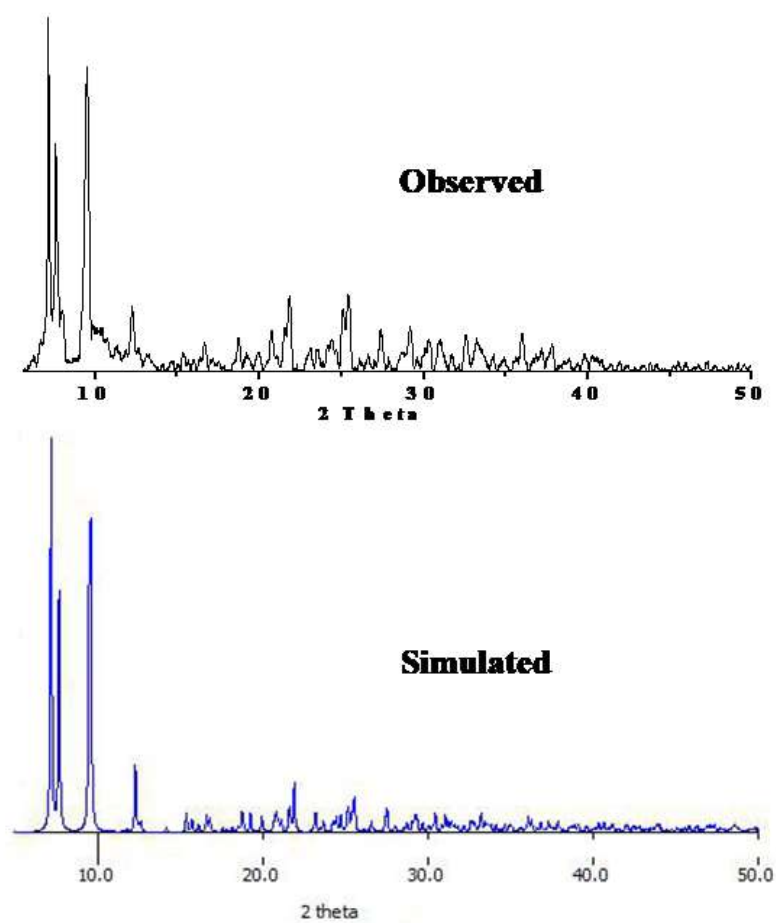
Fig. S3. Simulated (blue) and observed (black) powder X-ray diffraction (PXRD) patterns of $[Dy^{III}_4L_4(\mu_3\text{-}OH)_2(propionate)_2(dmf)_2]$ **(3)**.
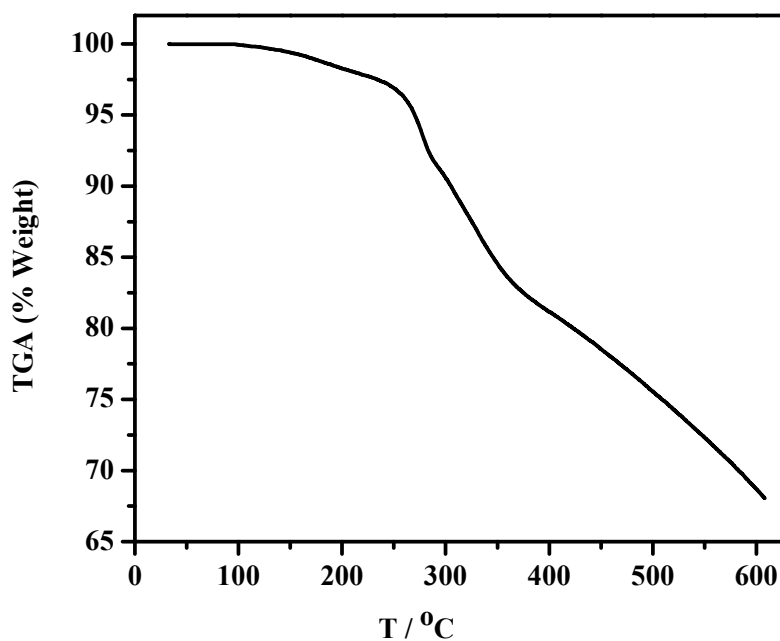
Fig. S4. Thermogravimetric analysis (TGA) curve of $[Dy^{III}{}_4L_4(\mu_3\text{-}OH)_2(acetate)_2(dmf)_2]$ **(2)** in nitrogen atmosphere.
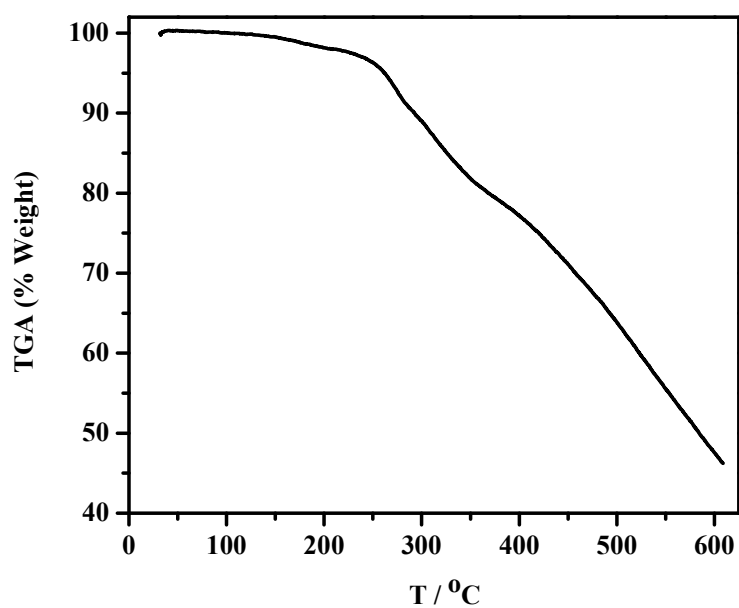
Fig. S5. Thermogravimetric analysis (TGA) curve of $[Dy^{III}{}_4L_4(\mu_3\text{-}OH)_2(propionate)_2(dmf)_2]$ **(3)** in nitrogen atmosphere.
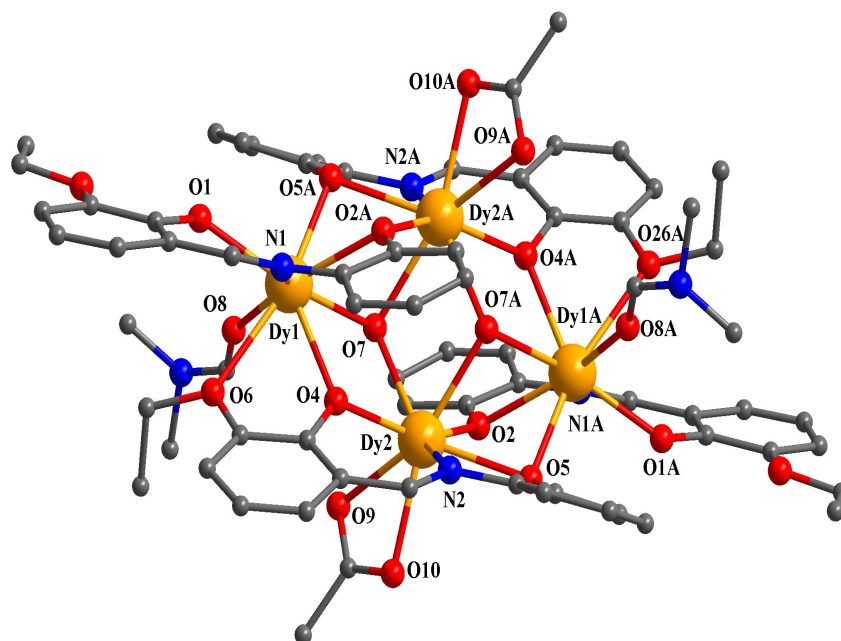
Fig. S6. Crystal structure of $[Dy^{III}_4L_4(\mu_3\text{-}OH)_2(acetate)_2(dmf)_2]$ (**2**). Hydrogen atoms are omitted for clarity. Symmetry code: A, 2–x, 2–y, 2–z.
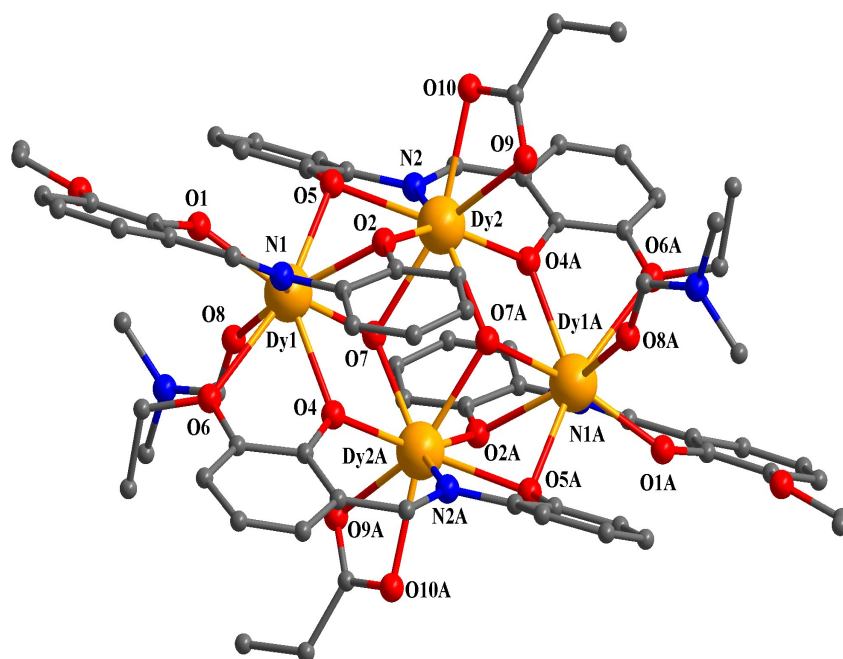
Fig. S7. Crystal structure of $[Dy^{III}_4L_4(\mu_3\text{-}OH)_2(propionate)_2(dmf)_2]$ (**3**). Hydrogen atoms are omitted for clarity. Symmetry code: A, 1–x, 2–y, 2–z.
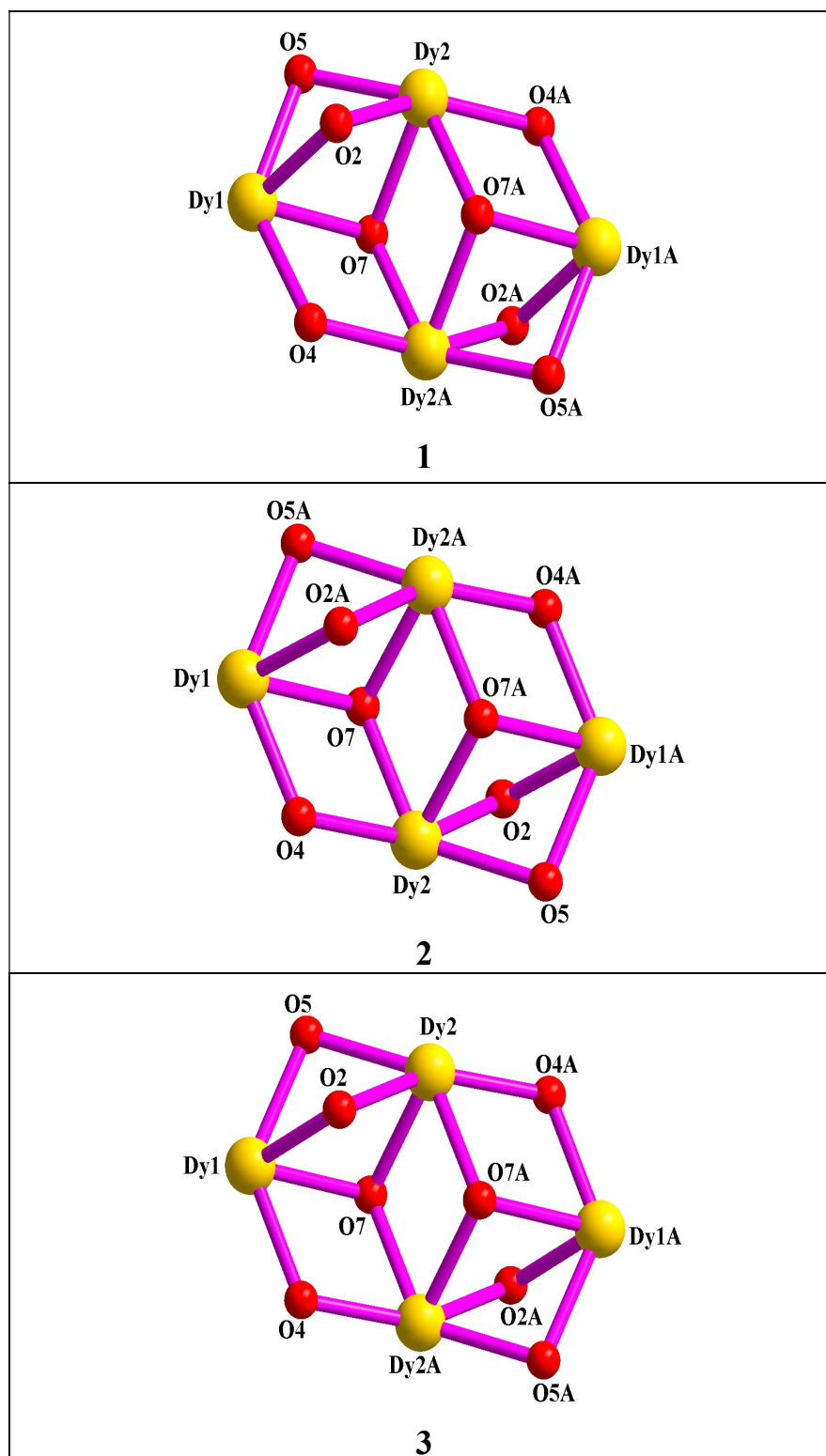
Fig. S8. Perspective views showing defect dicubane DyO_8 core in **1**, **2** and **3** (O_8 represents eight bridging phenoxo and hydroxo oxygen atoms). Symmetry code: A, 1−x, 2−y, 2−z.
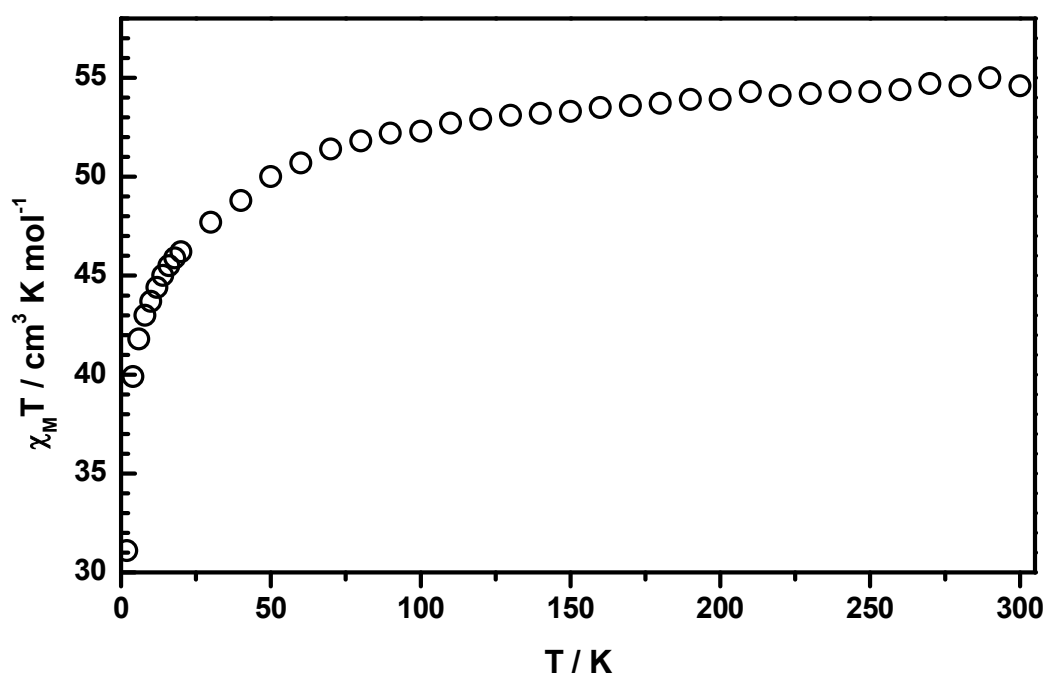
Fig. S9. Temperature dependence of the magnetic susceptibility in $\chi_M T$ vs T for [Dy^{III}$_4$L$_4$(μ_3-OH)$_2$(acetate)$_2$(dmf)$_2$] (**2**).
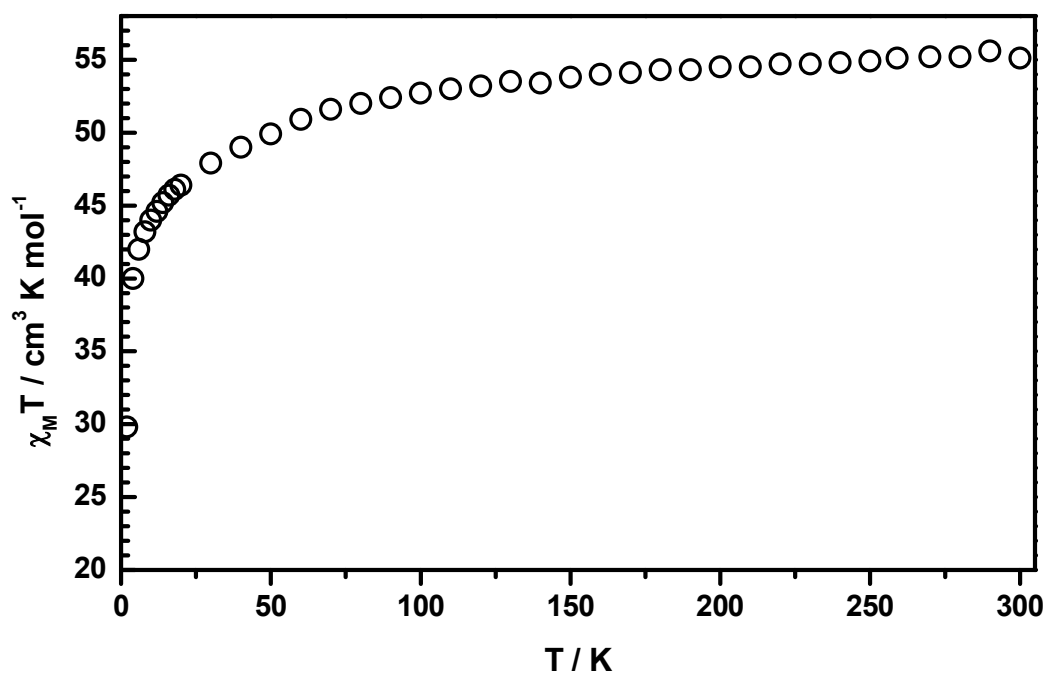
Fig. S10. Temperature dependence of the magnetic susceptibility in $\chi_M T$ vs T for [Dy^{III}$_4$L$_4$(μ_3-OH)$_2$(propionate)$_2$(dmf)$_2$] (**3**).
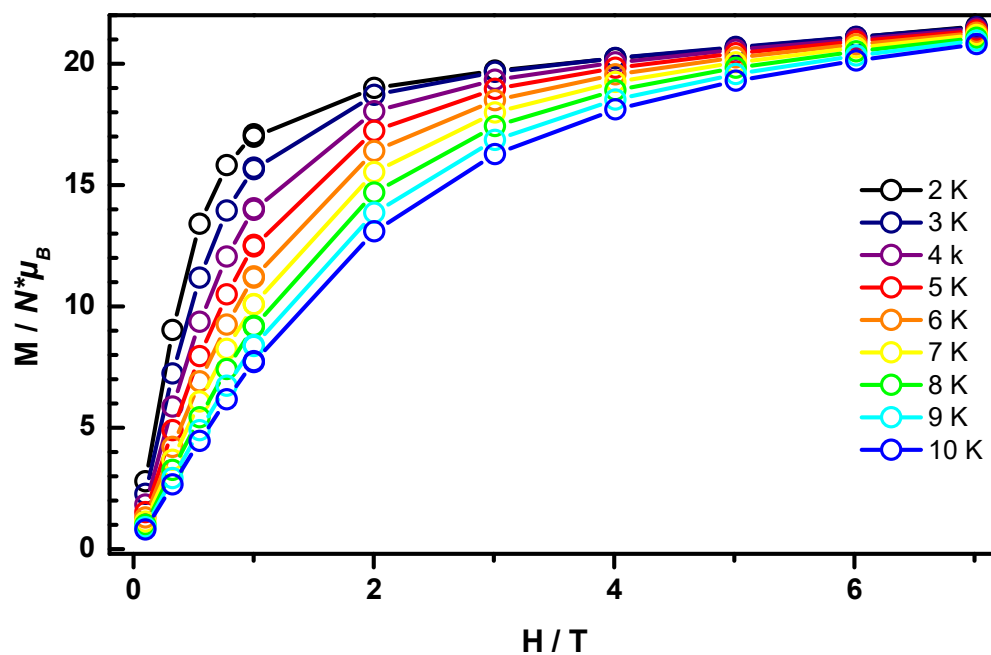
Fig. S11. Magnetization of [Dy$^{III}_4$L$_4$(μ_3-OH)$_2$(acetate)$_2$(dmf)$_2$] (**2**) in M vs H. The solid lines are guidelines for eyes.
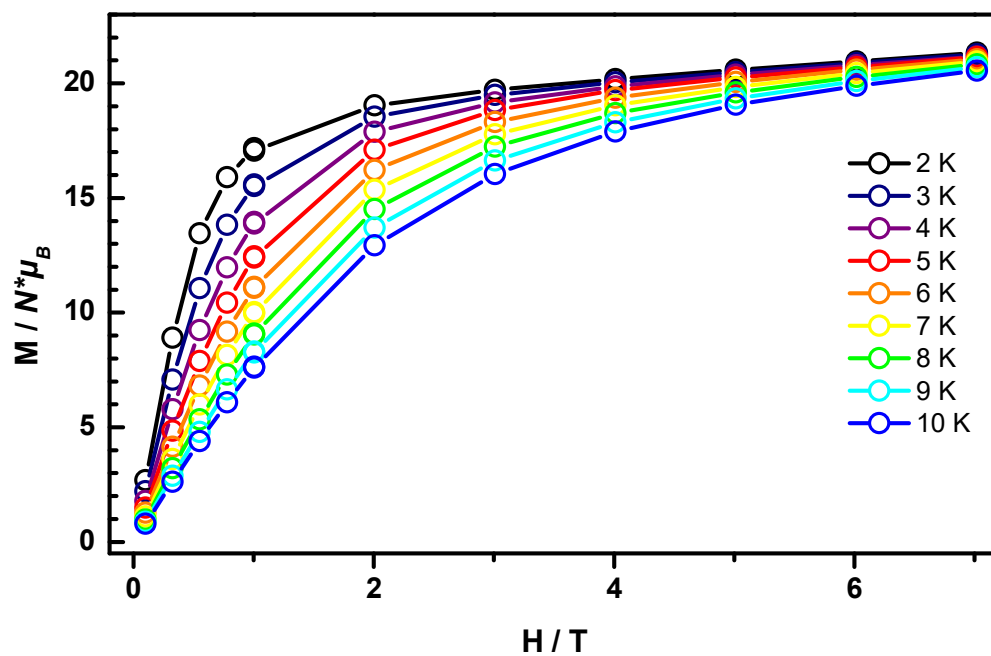
Fig. S12. Magnetization of [Dy$^{III}_4$L$_4$(μ_3-OH)$_2$(propionate)$_2$(dmf)$_2$] (**3**) in M vs H. The solid lines are guidelines for eyes.
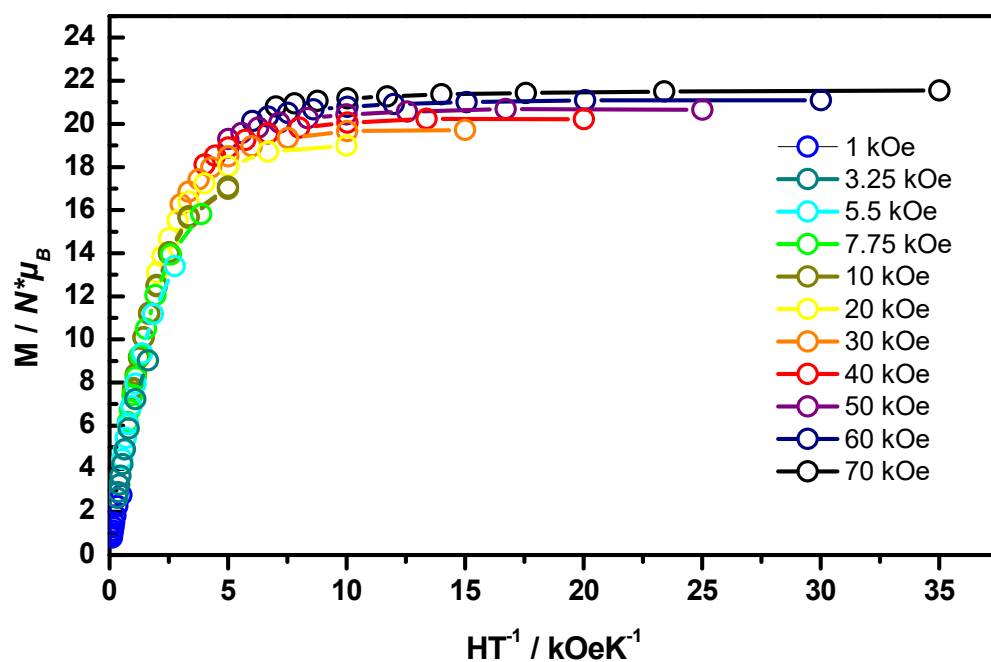
Fig. S13. Reduced magnetization of [Dy$^{III}_4$L$_4$(μ_3-OH)$_2$(acetate)$_2$(dmf)$_2$] (**2**) in M vs HT^{-1}. The solid lines are guidelines for eyes.
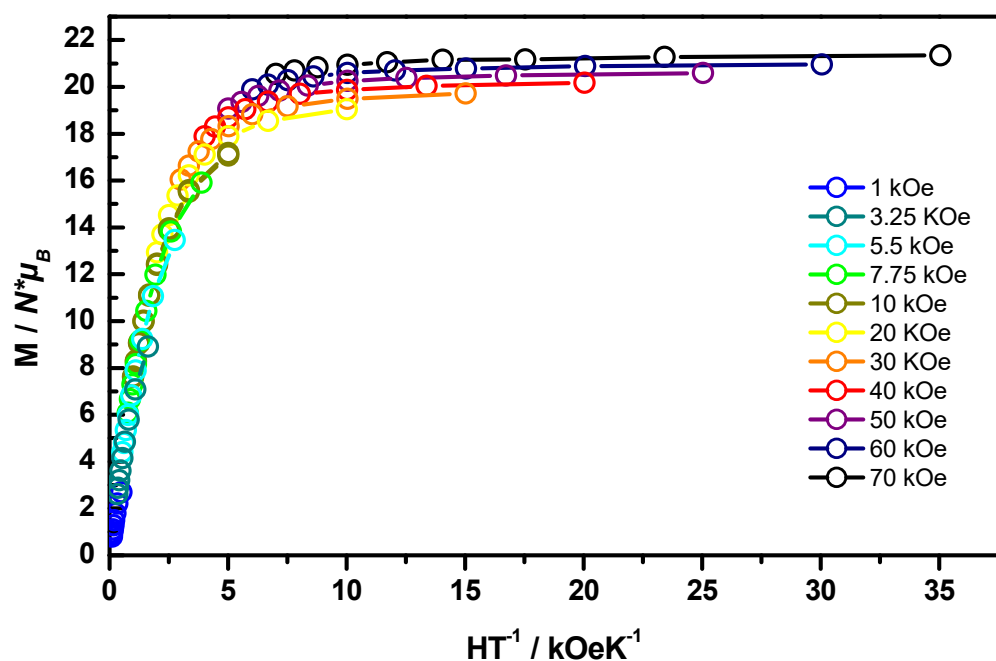
Fig. S14. Reduced magnetization of [Dy$^{III}_4$L$_4$(μ_3-OH)$_2$(propionate)$_2$(dmf)$_2$] (**3**) in M vs HT^{-1}. The solid lines are guidelines for eyes.
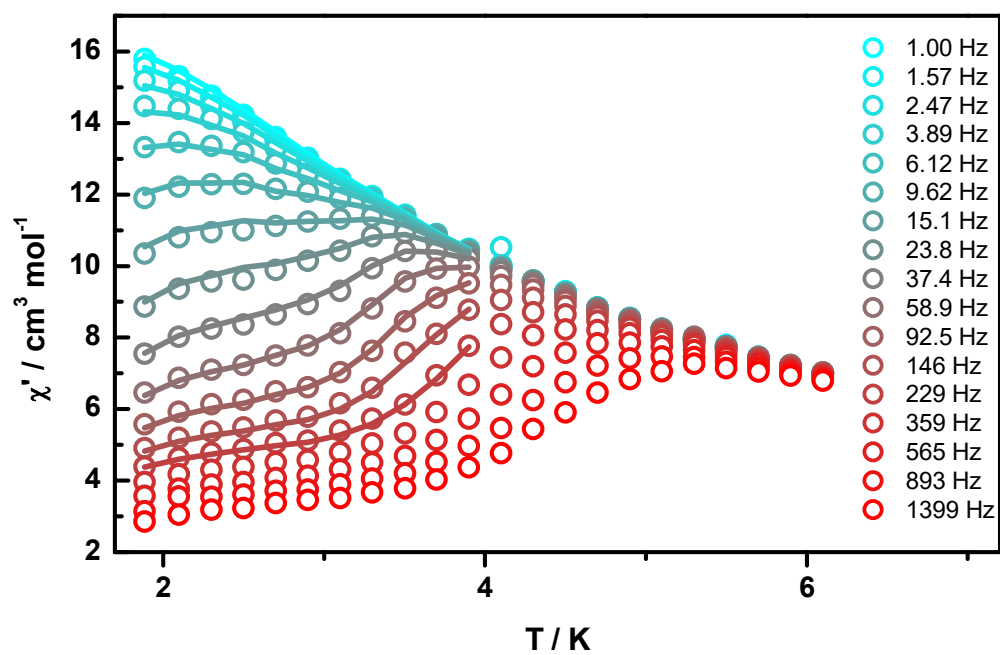
Fig. S15. Plots of the in-phase signal vs T at different frequencies for $[Dy^{III}_4L_4(\mu_3\text{-}OH)_2(\text{acetate})_2(\text{dmf})_2]$ (**2**). Solid lines correspond to the best fit.
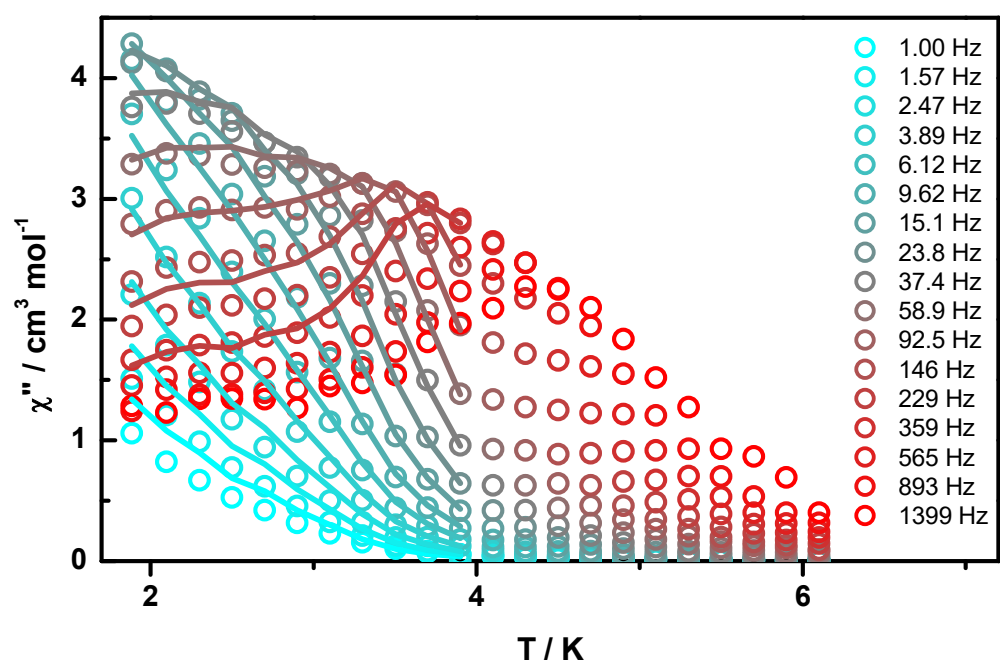
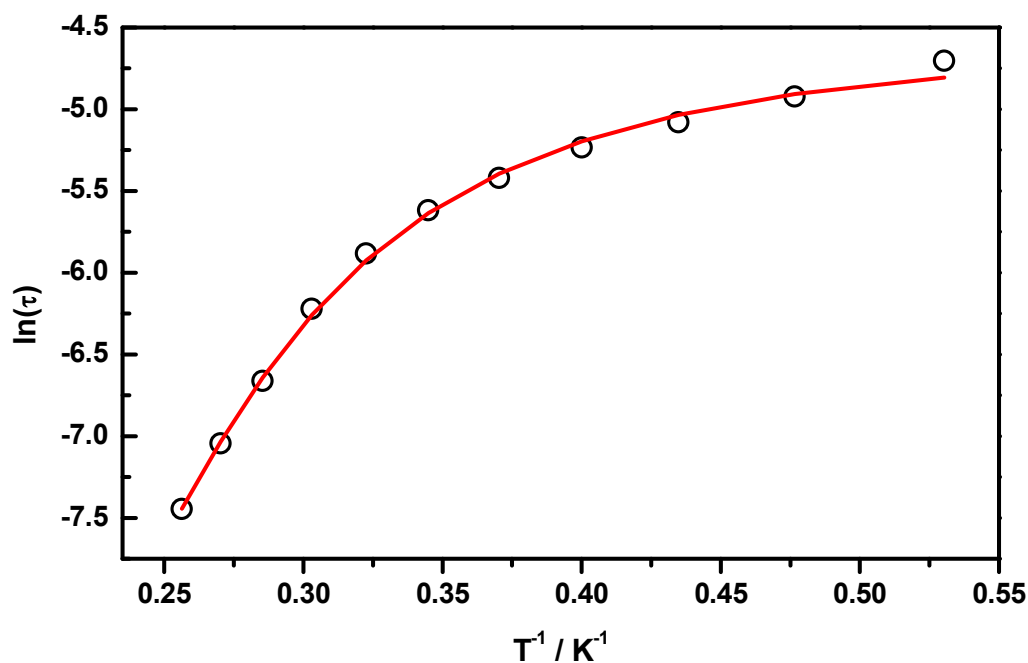**Fig. S16.** Plots of the out-of-phase signal vs T at different frequencies for $[Dy^{III}_4L_4(\mu_3\text{-}OH)_2(\text{acetate})_2(\text{dmf})_2]$ (**2**). Solid lines correspond to the best fit.
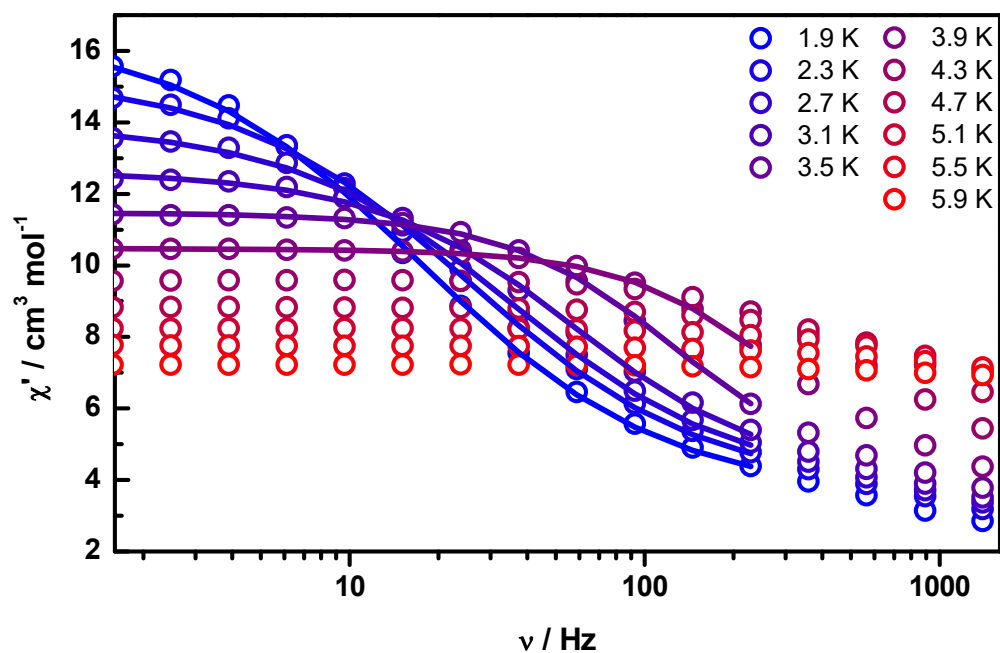
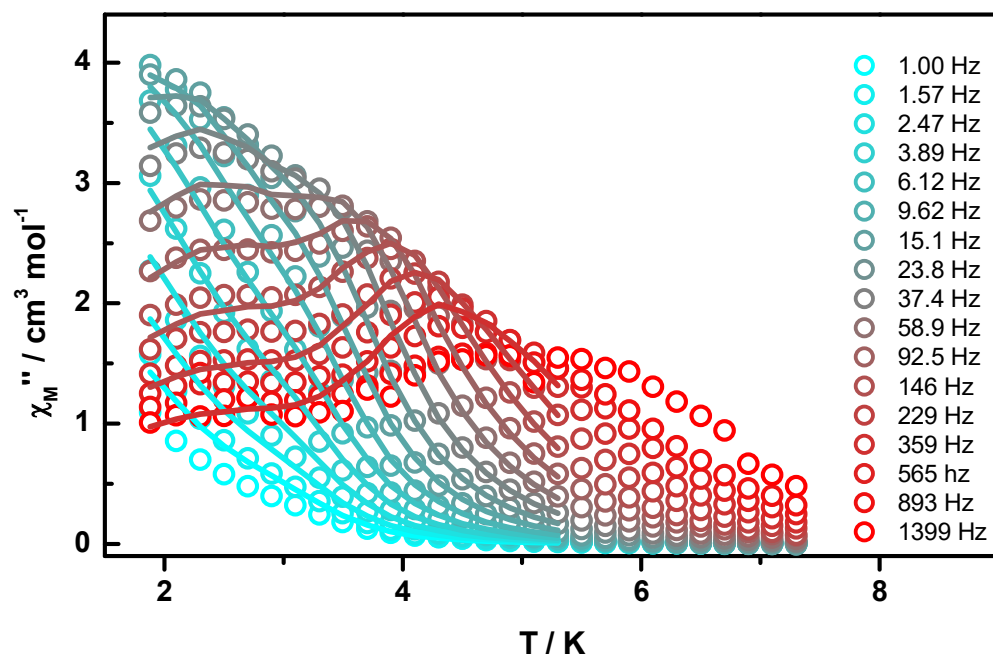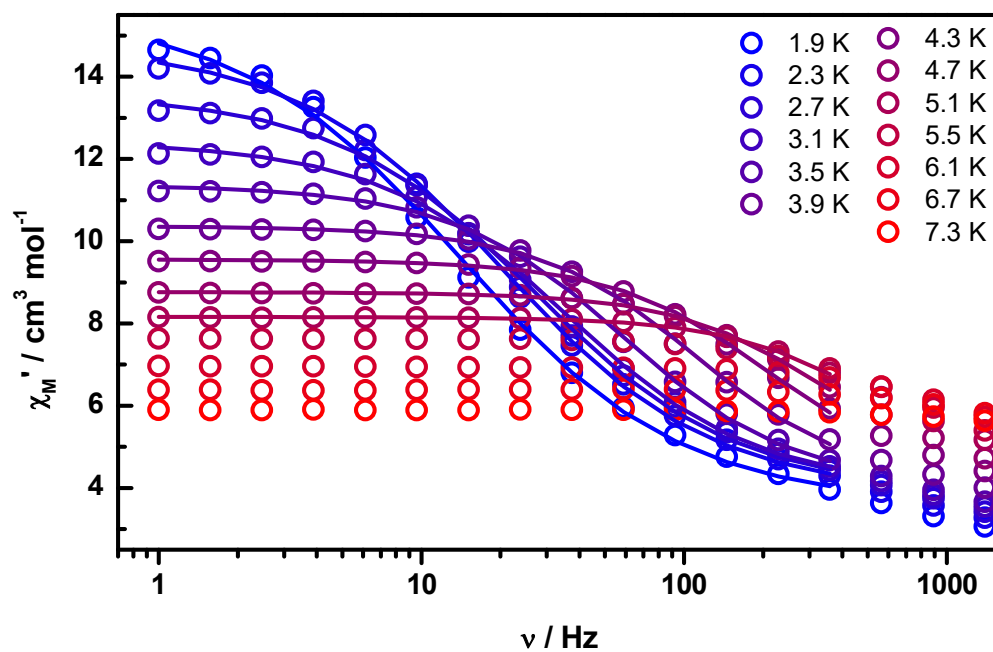**Fig. S17.** Plots of the in-phase signal vs ν at selected temperatures (Δ 0.4 K) for [Dy$^{III}_4$L$_4$(μ_3-OH)$_2$(acetate)$_2$(dmf)$_2$] (**2**). Solid lines correspond to the best fit.
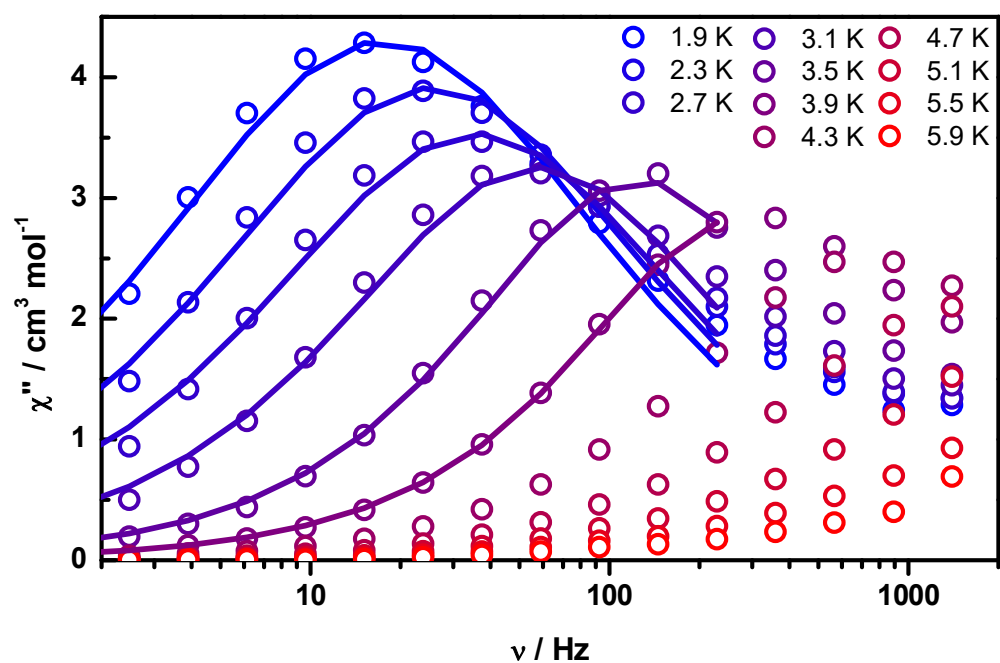
Fig. S18. Plots of the out-of-phase signal vs ν at selected temperatures (Δ 0.4 K) for [Dy$^{III}_4$L$_4$(μ_3-OH)$_2$(acetate)$_2$(dmf)$_2$] (**2**. Solid lines correspond to the best fit.
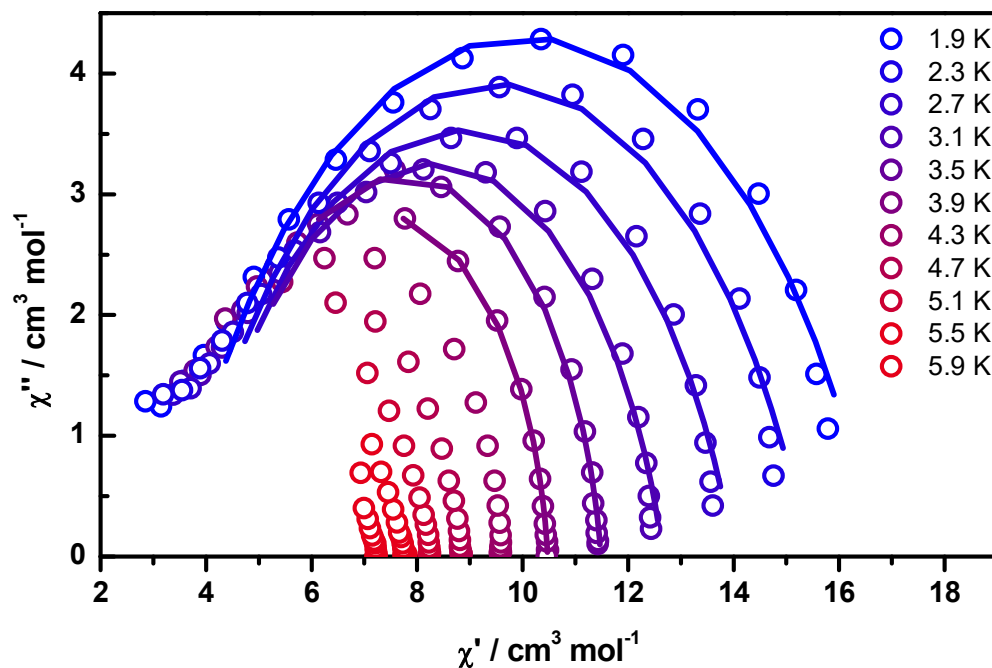
Fig. S19. Cole-Cole plots of the out-of-phase signal vs the in-phase signal at selected temperatures (Δ 0.4 K) for $[Dy^{III}_4L_4(\mu_3\text{-}OH)_2(acetate)_2(dmf)_2]$ (**2**). Solid lines correspond to the best fit.

Fig. S20. Plot of the natural logarithm of the relaxation time versus the reciprocal temperature for $[Dy^{III}_4L_4(\mu_3\text{-}OH)_2(acetate)_2(dmf)_2]$ (**2**). Solid lines correspond to the best fit with the values given in the text.
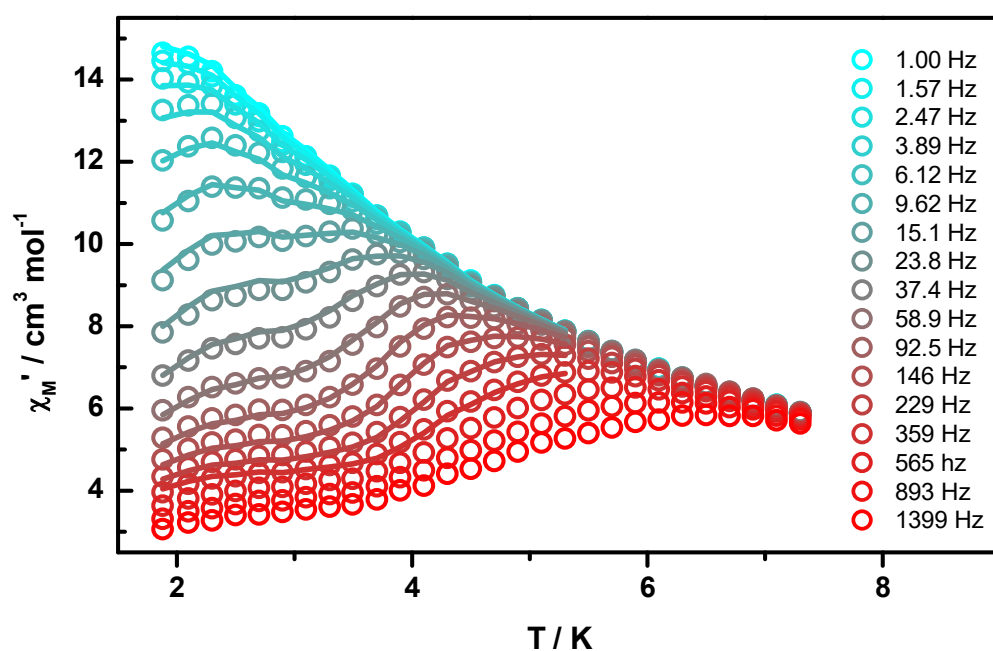
Fig. S21. Plots of the in-phase signal vs T at different frequencies for $[Dy^{III}_4L_4(\mu_3\text{-}OH)_2(propionate)_2(dmf)_2]$ (**3**). Solid lines correspond to the best fit.

Fig. S22. Plots of the out-of-phase signal vs T at different frequencies for $[Dy^{III}_4L_4(\mu_3\text{-}OH)_2(propionate)_2(dmf)_2]$ (**3**). Solid lines correspond to the best fit.

Fig. S23. Plots of the in-phase signal vs ν at selected temperatures (Δ 0.4 K) for $[Dy^{III}_4L_4(\mu_3\text{-}OH)_2(propionate)_2(dmf)_2]$ (**3**). Solid lines correspond to the best fit.
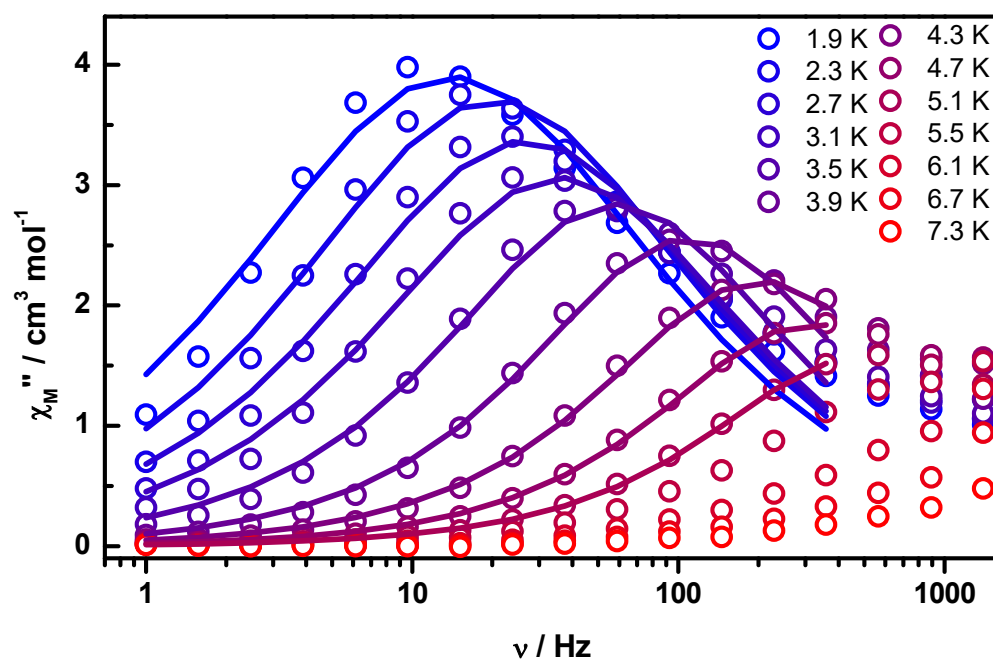
Fig. S24. Plots of the out-of-phase signal vs ν at selected temperatures (Δ 0.4 K) for $[Dy^{III}_4L_4(\mu_3\text{-}OH)_2(propionate)_2(dmf)_2]$ (**3**). Solid lines correspond to the best fit.
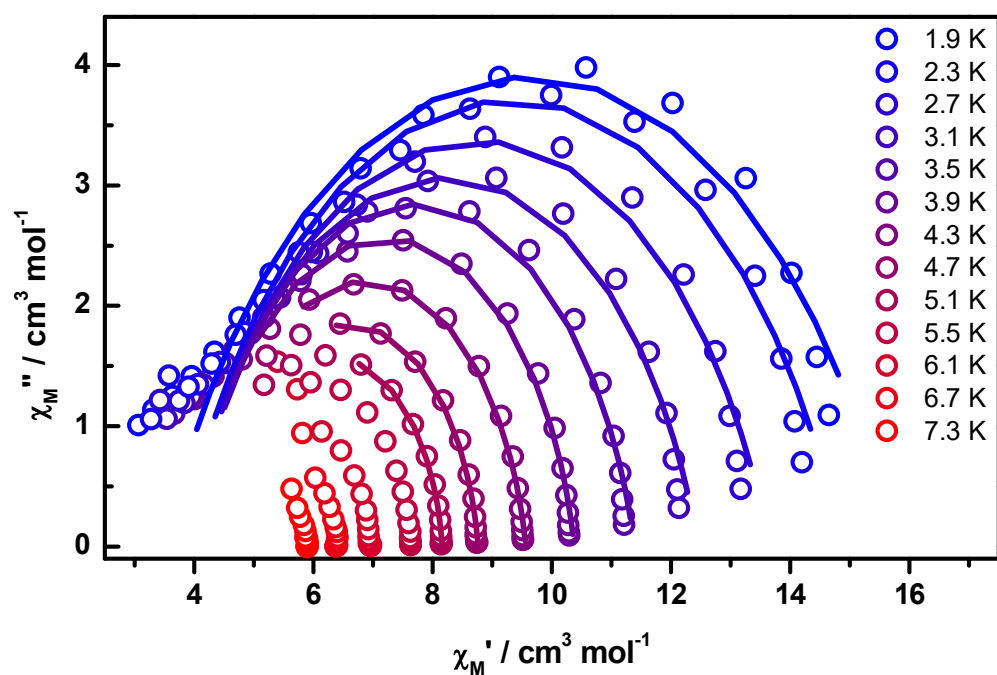
Fig. S25. Cole-Cole Plots of the out-of-phase signal vs the in-phase signal at selected temperatures (Δ 0.4 K) for $[Dy^{III}_4L_4(\mu_3-OH)_2(propionate)_2(dmf)_2]$ (**3**). Solid lines correspond to the best fit.
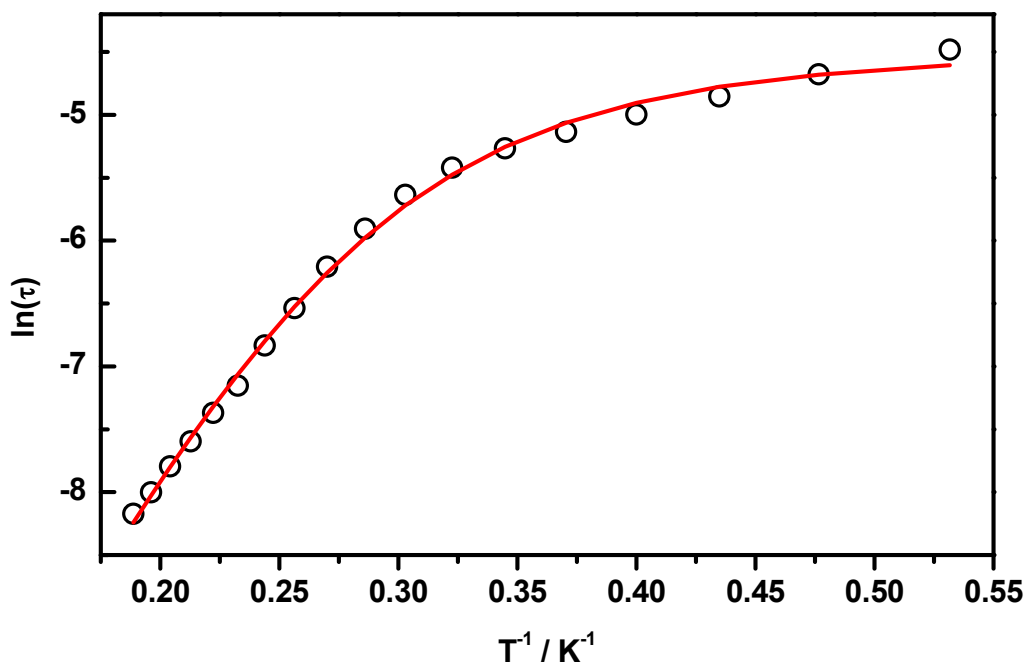

Fig. S26. Plot of the natural logarithm of the relaxation time versus the reciprocal temperature for $[Dy^{III}_4L_4(\mu_3-OH)_2(propionate)_2(dmf)_2]$ (**3**). Solid lines correspond to the best fit with the values given in the text.
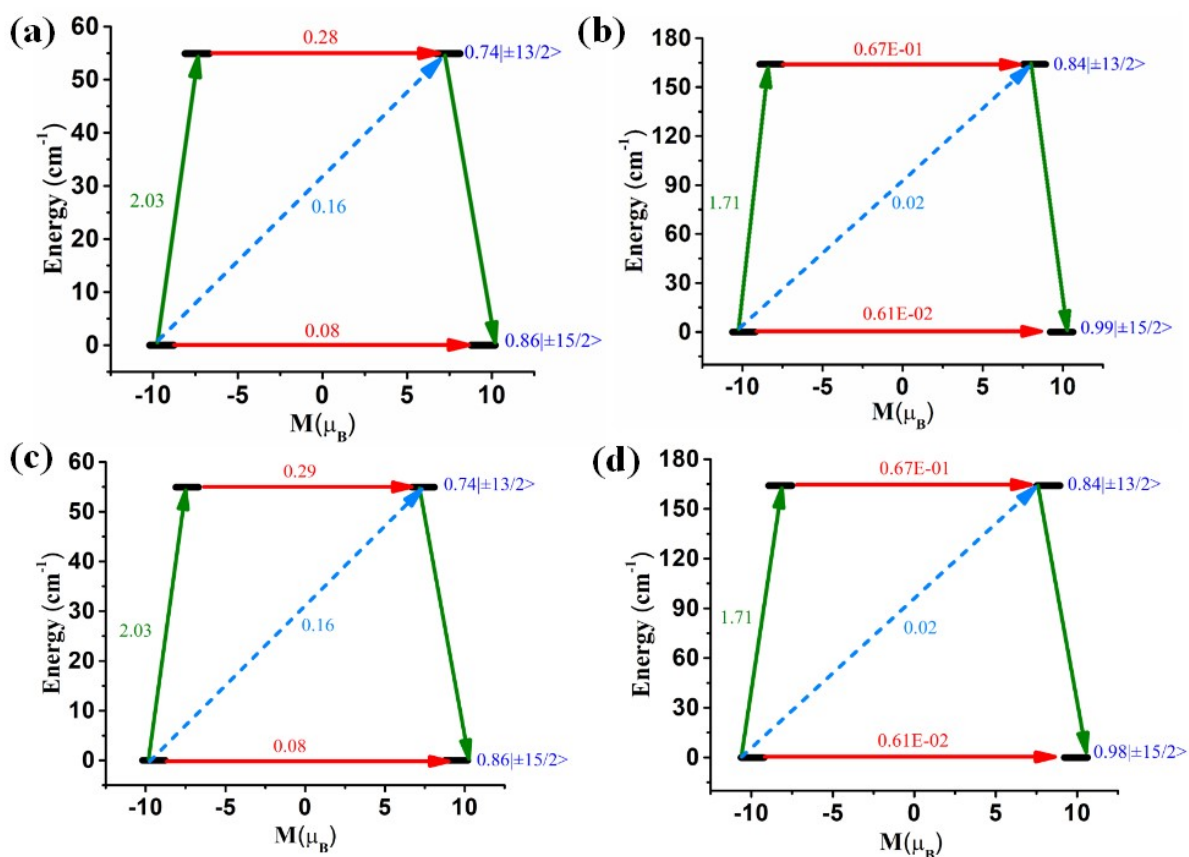
Fig. S27. The mechanism of magnetization relaxation of (a) Dy2A (Fig. S8; Dy_b) (b) Dy1 (Fig. S8; Dy_w) (c) Dy2 (Fig. S8; Dy_b) (d) Dy1A (Fig. S8; Dy_w) centres of complex **1**. The black level corresponds to the energy of a KD as a function of magnetic moment. The red arrow represents the QTM in the ground state and TA-QTM in the excited state. The sky-blue dashed arrow denotes the Orbach relaxation process and olive arrow denotes the most probable pathway of magnetization relaxation. The blue numbers represent the m_J composition of a KD.
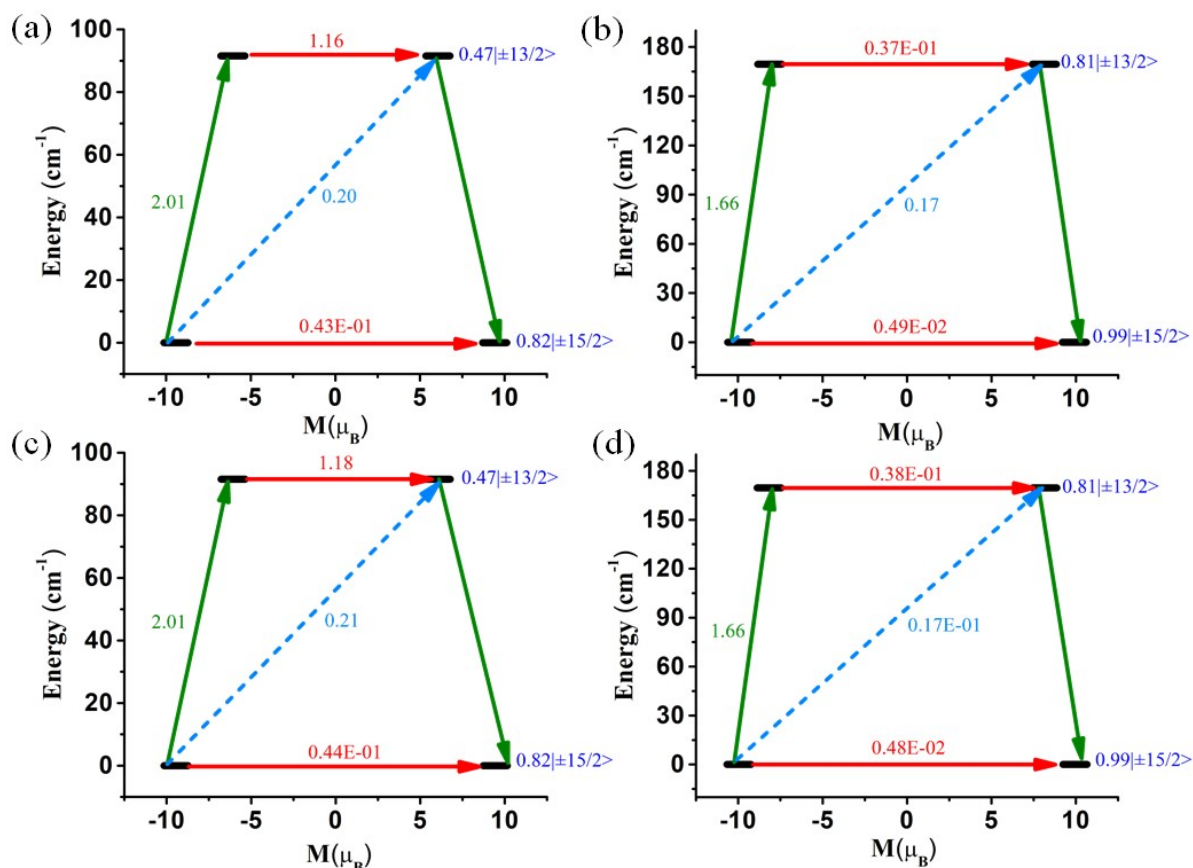
Fig. S28. The mechanism of magnetization relaxation of (a) Dy2 (Fig. S8; Dy$_b$) (b) Dy1 (Fig. S8; Dy$_w$) (c) Dy2A (Fig. S8; Dy$_b$) (d) Dy1A (Fig. S8; Dy$_w$) centres of complex **2**. The black level corresponds to the energy of a KD as a function of magnetic moment. The red arrow represents the QTM in the ground state and TA-QTM in the excited state. The sky-blue dashed arrow denotes the Orbach relaxation process and olive arrow denotes the most probable pathway of magnetization relaxation. The blue numbers represent the m_J composition of a KD.
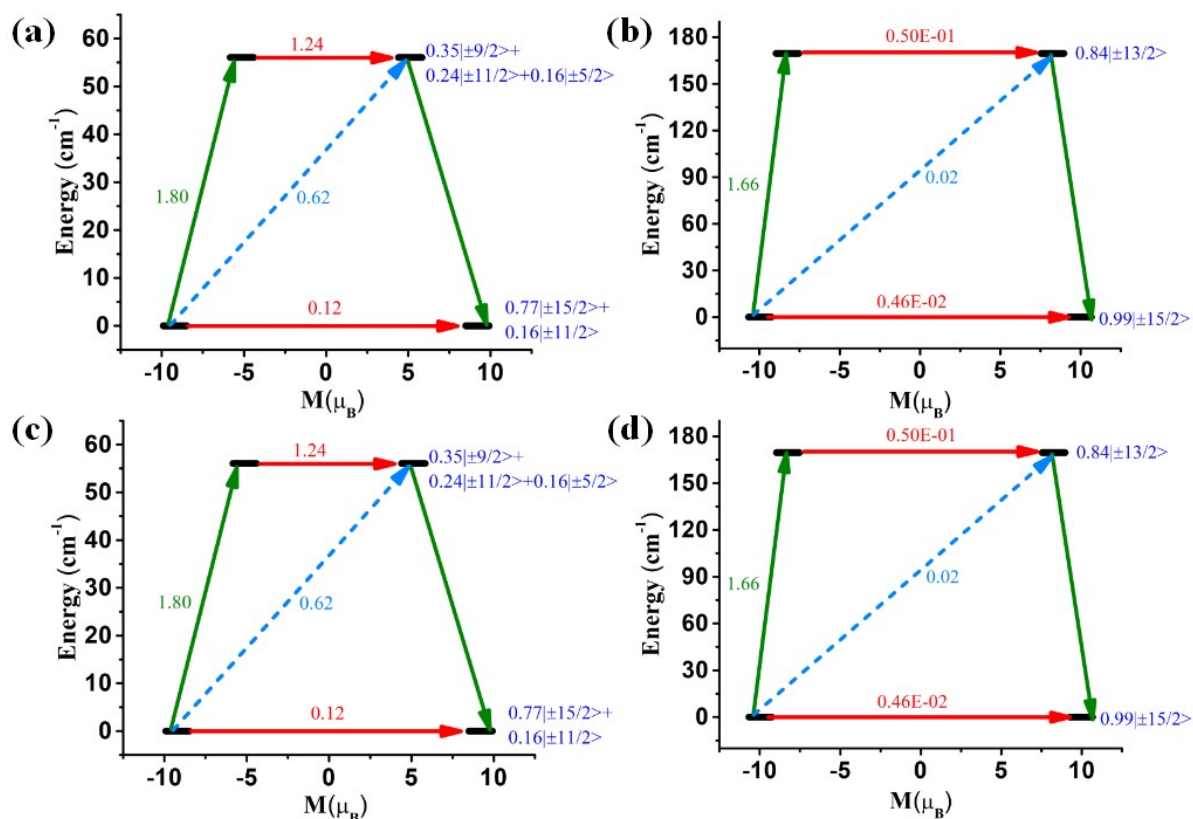
Fig. S29. The mechanism of magnetization relaxation of (a) Dy2A (Fig. S8; Dy_b) (b) Dy1 (Fig. S8; Dy_w) (c) Dy2 (Fig. S8; Dy_b) (d) Dy1A (Fig. S8; Dy_w) centres of complex **3**. The black level corresponds to the energy of a KD as a function of magnetic moment. The red arrow represents the QTM in the ground state and TA-QTM in the excited state. The sky-blue dashed arrow denotes the Orbach relaxation process and olive arrow denotes the most probable pathway of magnetization relaxation. The blue numbers represent the m_J composition of a KD.
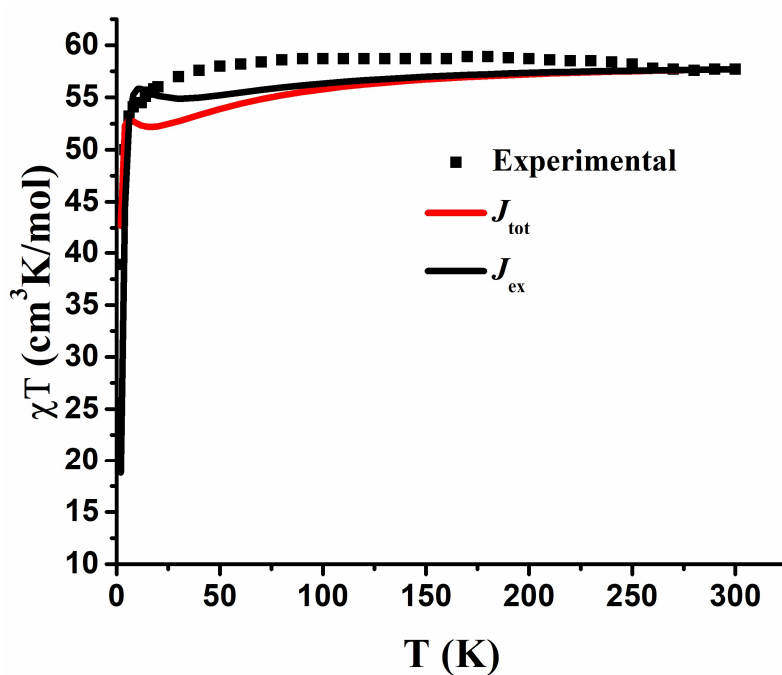
Fig. S30. A comparison of experimental and POLY_ANISO simulated χT vs T plot of complex **2**.
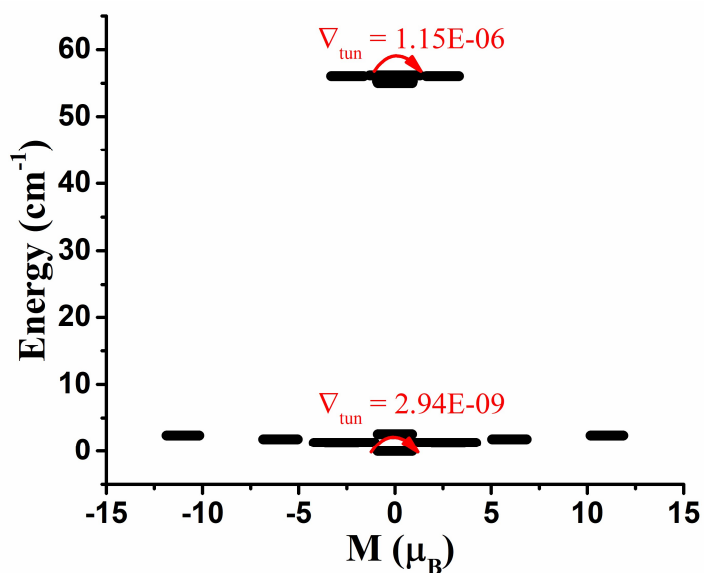

Fig. S31. The exchange coupled relaxation mechanism of complex **1**. The black line indicated the energy of pKD as a function of magnetic moment. The tunnel splitting (∇_{tun}) values are given in cm^{-1}.

References:

S1.   K. Zhang, V. Montigaud, O. Cador, G.-P. Li, B. L. Guennic, J.-K. Tang and Y.-Y. Wang, *Inorg. Chem*., 2018, **57**, 8550.

S2.   K. Zhang, G.-P. Li, C. Zhang and Y.-Y. Wang, *J. Soild State Chem*., 2019, **273**, 11.

S3.   K. Zhang, G.-P. Li, V. Montigaud, O. Cador, B. L. Guennic, J.-K. Tang and Y.-Y. Wang, *Dalton Trans*., 2019, **48**, 2135.

S4.   K. C. Mondal, G. E. Kostakis, Y. Lan and A. K. Powell, *Polyhedron*, 2013, **66**, 268.

S5.   A. K. Jami, J. Ali, S. Mondal, J. Homs-Esquius, E. C. Sañudo and V. Baskar, *Polyhedron*, 2018, **151**, 90.